

## On the reliability of 3D gel dosimetry

This content has been downloaded from IOPscience. Please scroll down to see the full text.

2013 J. Phys.: Conf. Ser. 444 012015

(<http://iopscience.iop.org/1742-6596/444/1/012015>)

View the [table of contents for this issue](#), or go to the [journal homepage](#) for more

Download details:

IP Address: 76.75.148.30

This content was downloaded on 06/02/2015 at 19:12

Please note that [terms and conditions apply](#).

# On the reliability of 3D gel dosimetry

**Y De Deene<sup>1,2</sup> and J Vandecasteele<sup>2</sup>**

<sup>1</sup>Institute of Medical Physics, School of Physics, University of Sydney

<sup>2</sup>Department for Radiotherapy and Experimental Cancer Research, Ghent University Hospital, De Pintelaan 185, 9000 Gent, Belgium

E-mail: Yves.DeDeene@UGent.be

**Abstract.** Gel dosimetry has a unique role to play in safeguarding conformal radiotherapy treatments as it covers the whole treatment chain and provides the radiation oncologist with the integrated dose distribution in 3D. A major obstacle that has hindered the wider dissemination of polymer gel dosimetry in radiotherapy centres is the lack of confidence in the reliability of the measured dose. Discrepancies in dose response of small versus large polymer gel dosimeters have been reported and although several hypothesis for these discrepancies have been postulated, the actual contribution of these error sources to the overall inaccuracy of the dose maps has not been determined. Several gel dosimetry research groups have chosen to use an internal calibration of gel dosimeters. In this study, the inter-and intra-batch reproducibility of the current state-of-the-art 3D gel dosimeters has been assessed. It is demonstrated that with a carefully designed scanning set-up, the overall accuracy that can be obtained with an independent calibration is well within 5% of all pixels.

## 1. Introduction

### 1.1. Gel dosimetry as a 3D dose verification method

Gel dosimetry provides a unique feature to display dose distributions occurring in clinical radiotherapy in three dimensions (3D) in humanoid shaped phantoms [1-3]. It has a unique role to play in safeguarding conformal radiotherapy treatments as it is the only dosimeter that covers the whole treatment chain and provides the radiation oncologist with the integrated dose distribution in 3D. However, some doubts with respect to the overall reliability have overshadowed the wider dissemination of polymer gel dosimetry in radiation centers. Significant differences in dose-R<sub>2</sub> response have been found between gel dosimeters that were poured in small calibration vials as compared to larger phantom recipients [4,5]. This finding severely compromises the use of an externally derived calibration curve to convert the measured R<sub>2</sub> maps to dose maps. Several possible reasons have been proposed as explanation for the observed discrepancies such as differences in cooling rate [6], changes in temperature during irradiation as result of the exothermal radiation induced polymerization reaction [7] and physicochemical changes related to an oxygen-antioxidant imbalance [8]. To circumvent the discrepancies in dose-R<sub>2</sub> response between small test tubes and larger volumetric anthropomorphic gel dosimeter phantoms many researchers have chosen to apply an internal calibration (i.e. the R<sub>2</sub> is calibrated to dose by using two points within the phantom as ‘known’ doses). Regardless the fact that with an internal calibration, the ability of gel dosimetry to safeguard absolute dose information of a treatment is lost, it should also be emphasized that there is a potential



Content from this work may be used under the terms of the [Creative Commons Attribution 3.0 licence](#). Any further distribution of this work must maintain attribution to the author(s) and the title of the work, journal citation and DOI.

more severe danger with this strategy because the mentioned mechanisms may depend on radiation dose, dose rate, environmental conditions and size and shape of the phantom. There is therefore no evidence that the same mechanism for the observed discrepancies would not cause any dose read errors within the volumetric polymer gel dosimeter phantom itself.

The evaluation methods that have been applied by many gel dosimetry research groups to give evidence of the ‘potential’ of gel dosimetry are often based on a percentage number of pixels that pass gamma criteria between a gel dosimetry (GD) measured dose distribution and a treatment planning system (TPS) calculated dose distribution. This value obviously depends on the number of slices and the size (field-of-view) of the dose maps taken into consideration. Although it is recognized that gamma maps are a valuable tool in benchmarking a radiotherapy treatment plan, the use of a percentage value of passing pixels in benchmarking a dosimetry technique against a TPS calculated dose distribution can be misleading as proof of the reliability of the dosimetry technique. Moreover, it is not beyond discussion to what extend a TPS calculated dose distribution should be used as ‘golden standard’ to benchmark a new dosimeter. Of course, it is recognized that the intrinsic problem with the benchmarking of a 3D dosimeter is that there does not exist a 3D dosimetric ‘golden standard’ to compare with. The most reasonable strategy is to compare doses obtained with gel dosimetry with doses obtained by the most reliable dosimetry techniques that apply to a certain spatial dimension. For example, dose profiles of a single field (photons and electrons) can be compared with dose profiles obtained with an ionization chamber or diamond detector [9,10]. In two dimensions, gel dosimetry can be compared with film dosimetry [3,9,11]. Dose distributions obtained with gel dosimetry have been compared with those calculated with treatment planning software [3, 12-18]. Errors that compromise the accuracy may occur at different stages of the dosimetry procedure [19]. Given the uncertainties with respect to the dose- $R_2$  response, we argue that a more stringent criterion than gamma criteria should be applied for benchmarking 3D gel dosimetry.

### 1.2. Accuracy and precision

In this perspective it may be helpful to refresh the definition of accuracy and precision: *Accuracy* can be defined as the degree of conformity of a measured or calculated quantity (measurand) to its actual (true) value. *Precision* can be defined as the ability of a measurement to be consistently reproduced. Accuracy and precision can be defined statistically in terms of the deviation of the mean value from the reference value and the standard deviation of the mean value of many measurements respectively (figure 1). The measurement uncertainty of a single experiment thus comprises both systematic and random errors. Uncertainties have later been reclassified in type A and type B uncertainties where type A standard uncertainty is obtained from a probability density function derived from an observed frequency distribution, while type B standard uncertainty is obtained from an assumed probability density function that is bases on the degree of belief that an event will occur.

In the case of gel dosimetry, uncertainty applies to both dose and space. In a gel dosimetry dose verification experiment (and any radiation treatment), the spatial and dosimetric dimensions are interwoven. It is theoretically impossible to extract both dosimetric and spatial errors from a measured spatial dose distribution (i.e. the result of a 3D gel dosimetry experiment). To comprise both spatial and dosimetric performance in one parameter, Low *et al* have introduced the gamma-index [20]. Other dose distribution comparisons are performed on the basis of maximum allowed dose differences [21].

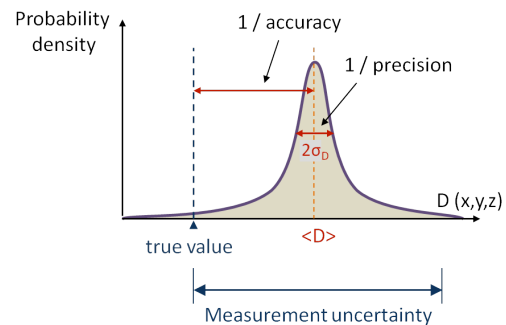


**Figure 1.** Accuracy and precision shown schematically in terms of probabilities of occurrence. Precision can be characterised in terms of the standard deviation of many measurements (experiments). The accuracy is characterized by the deviation of the mean of many measurements from the reference value.

To obtain a picture of the overall uncertainty of polymer gel dosimetry, also the fabrication and irradiation have to be included in the analysis. This can be achieved through a reproducibility study of the complete gel dosimetry experiment from gel fabrication to dose distribution analysis. An extensive reproducibility study, comprising the repetition of a gel dosimetry experiment 8 times, is proposed in this review and the contributions of different sources of inaccuracy are discussed. It is imperative to realize that in a clinical verification with gel dosimetry, consisting of a single experiment, the uncertainty of the dose measured in each voxel comprises both the systematic inaccuracy as the imprecision.

Gel dosimetry is performed in different steps and errors can occur at each stage (figure 2): (1) The polymer gel dosimeter is fabricated in a chemical laboratory and is stored until radiation. Any deviations in the chemical composition through inhomogeneous mixing, impurities in the recipients or oxygen leaks in the recipient can give rise to discrepancies between calibration tubes and volumetric phantoms [8]. Moreover, a difference in temperature course during storage may also affect the dose-R2 response [6]. Most of these deviations are compensated by using calibration phantoms that are fabricated from the same batch of gel. (2) The gel dosimeter phantom is then scanned with CT and the treatment planning is optimized (3) on the scanned set for a virtual planning target volume (PTV) and a set of critical organs. At this stage, just as with a patient, a reference coordinate system is allocated to the phantom by use of marker lines that are drawn on the phantom. In addition, stereotactic fixtures or fiducial markers [22] can be placed on the phantom that will later be visible on the MRI images or optical images and CT images in the case of optical or X-ray CT readout respectively for coregistration of the dose maps with the TPS. Positional setup errors are likely to result in deviations between the planned and the measured dose distribution. These deviations are not intrinsic to the gel dosimeter but are indicative for errors that may occur during the actual patient treatment. (4) Upon irradiation, a complex set of radiation-induced chemical reactions take place. On a molecular level, these reactions are probabilistic in nature.

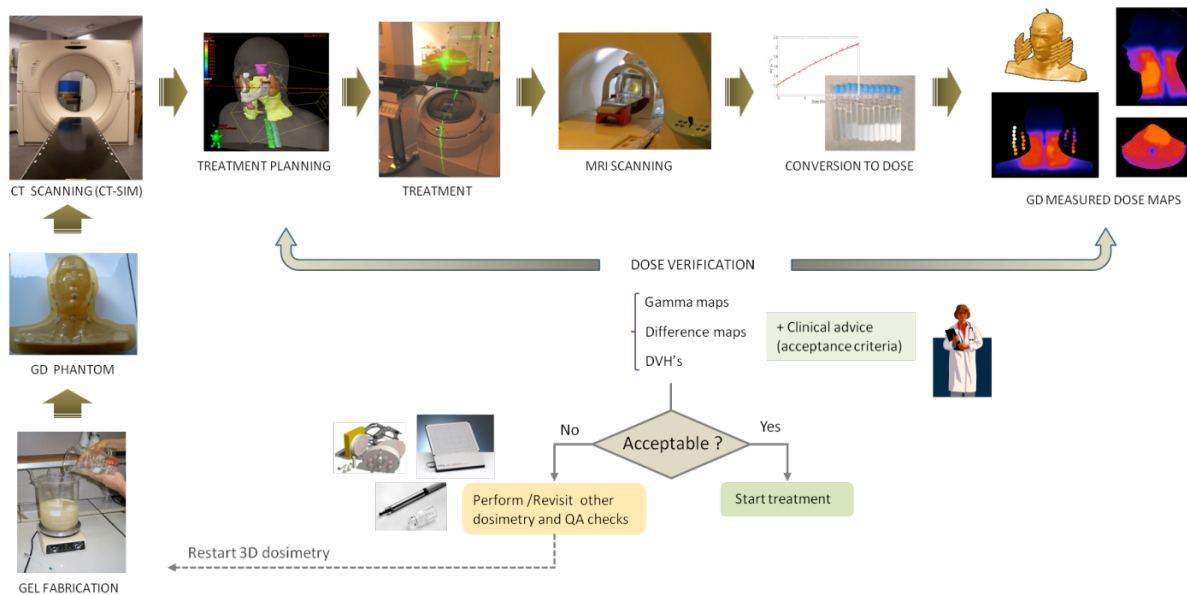


**Figure 2.** In treatment verification with gel dosimetry, the gel dosimeter phantom is taken through the entire treatment chain. Possible dosimetric or setup errors can occur at the different stages.

In most gel dosimetry applications, the voxel-size is several orders of magnitude bigger than the molecular size. As a result, this intrinsic radiochemical noise contribution can be easily neglected. Any positional set-up errors in treatment with respect to the planned treatment will affect the dose distribution. This error may also occur in patient treatment and is therefore not intrinsic to gel

dosimetry (GD). In benchmarking GD however, the experimental set-up error should be minimized as much as possible.

Other sources of deviation in dose reading that may occur during irradiation of the gel dosimeter are related to the dependence of the irradiation response on the temperature of the 3D dosimeter during irradiation, on the dose rate and on the energy spectrum of the irradiation beam [23,24]. It is important to realize that differences in dose rate (and energy) will occur in the irradiated 3D volume even if the photon fluence rate (in terms of MU/min) of the individual beams is kept constant. Another important characteristic of the gel dosimeter is its temporal and spatial integrity [25]. These errors are inherent to the gel dosimeter and should be minimized in a good dosimeter as they compromise the specificity of the dosimeter. After irradiation, the gel dosimeter is scanned (5). During scanning, thermal noise will add to the measurements. In order to minimize the noise in the measured dose distribution the scanning parameters should be optimized [26,27]. The processing (fitting) of acquired data, may have a big influence on the amplification of the noise figure. For example, in quantitative R<sub>2</sub>-NMR scanning it is found that a least-square fit will amplify the thermal noise in the base images to a larger extent than a chi-square ( $\chi^2$ ) based minimization. Imaging artifacts may result in systematic errors both dosimetric as spatially.

**Table 1.** Factors that determine the uncertainty in 3D gel dosimetry, classified in type A and type B. Factors indicated in red italic font also affect patient treatment.

|           | Type A (random error)   | Type B (systematic error)   |   |   |
|-----------|---|---|---|---|
|           | Dosimetric  | Spatial   | Dosimetric  | Spatial   |
| Chemical  | <ul style="list-style-type: none"> <li>Variation in chemical concentration</li> <li>Manufacturing temperature</li> <li>Dose sensitivity</li> </ul>  |   | <ul style="list-style-type: none"> <li>Discrepancies between calibration vials and phantom</li> <li>Chemical stability</li> <li>Spatial integrity</li> </ul>  | <ul style="list-style-type: none"> <li>Volumetric contraction of the gel dosimeter</li> </ul> |
|           | <ul style="list-style-type: none"> <li><i>Stochastic variations in the delivered dose</i></li> <li>Variations in the temperature during radiation</li> <li>Reproducibility of calib. phantom-positioning</li> <li><i>Radiochemical noise</i></li> </ul> | <ul style="list-style-type: none"> <li><i>Variations in the phantom position</i></li> <li>Spatial temperature variations in combination with temp. sensitive dose response</li> </ul> | <ul style="list-style-type: none"> <li>Positioning error of the calibration phantom</li> <li>Dose-rate dependent response</li> <li>Energy-dependent response</li> <li>Temperature dependence</li> <li>Tissue equivalence</li> <li>Recipient wall effects</li> </ul> | <ul style="list-style-type: none"> <li>Phantom positioning error</li> </ul>                   |
| Radiation | <ul style="list-style-type: none"> <li>Thermal noise</li> </ul>   | <ul style="list-style-type: none"> <li>Voxel size / shape (resolution)</li> </ul>   | <ul style="list-style-type: none"> <li>Voxel shape (bandwidth)</li> <li>Imaging artefacts</li> <li>Temperature during scanning</li> </ul>   | <ul style="list-style-type: none"> <li>Imaging artefacts</li> </ul>                           |
|           |   |   |   |   |
| Scanning  |   |   |   |   |

## 2. Type A uncertainty

The overall dosimetric precision is compromised by stochastic variations (random errors) that result from the several operations that take place in the dosimetry experiment. The first step in a gel dosimetry experiment is weighting the chemicals. Stochastic variations in the weighting will result in variations in the measured dose-related value ( $R_2$ , MT, OD) as the dose-response is determined by the chemical composition. It is found that other manufacturing conditions may also have an influence on the dose-response such as the temperature during fabrication. Stochastic variations in the controlled temperature between different experiments will therefore also lead to variations in the measured dose-related value. Also during irradiation there are different sources of stochastic variable contributions that determine the overall dosimetric precision such as variations in the dose delivery, variations in the temperature during irradiation and stochastic variations in the positioning of the calibration phantoms. Any form of scanning the gel dosimeter will introduce thermal detector noise. The noise contribution is determined by some scan parameters. Often, the scan parameters can be optimized in order to achieve an optimal figure of precision. In gel dosimetry, a calibration of the scanned parametric map (e.g.  $R_2$  map) is needed to obtain a dose map. Any random errors and influence quantities that operate on the calibration samples will also affect the uncertainty of the dose map. Because the calibration vials and the volumetric gel dosimeter phantom are filled with gel having the same composition (same batch of gel), any random errors in weighting the chemicals will not result in a random variation in the final dose measurement. In addition, the stochastic variations in beam output during radiation of the calibration vials can also be assumed to be significantly less than 1% which is also supported by a reproducibility study where 20 (calibration) samples were irradiated with the same dose and under the same conditions. The resulting type A (random) uncertainty is therefore considered as only originating from thermal noise during scanning.

The concept of dose-resolution was introduced to evaluate *the intrinsic dosimetric precision* in terms of dose sensitivity and scanning signal-to-noise [44]. The dose resolution, written as  $D_{\Delta}^p$ , is defined as the minimal detectable dose difference within a given level of confidence,  $p$ . The dose resolution is related to the standard deviation on dose  $\sigma_D$  by the equation

$$D_{\Delta}^p = \sqrt{2} \cdot k_p \cdot \sigma_D \quad (1)$$

For a 95% confidence level, the dose resolution becomes  $D_{\Delta}^p = 2.77 \sigma_D$ .

In most radiation dosimetry experiments, gel dosimeters are used in a relative manner in the sense that the dosimeter is exposed to the same treatment as the patient but with a different total radiation dose. The total dose delivered to the dosimeter is scaled to cover the active dose range of the dosimeter. In this context, it is preferable to use the concept of dose resolution relative to the operating dose range, here defined as *relative dose resolution*  $D_{\Delta\%}^p$ :

$$D_{\Delta\%}^p = \frac{D_{\Delta}^p}{(D_{max} - D_{min})} = \sqrt{2} \cdot k_p \frac{\sigma_D}{(D_{max} - D_{min})} \quad (2)$$

If the dose maps are derived from quantitative NMR- $R_2$  maps, it can be shown that the relative dose resolution ( $D_{\Delta\%}^p$ ) is equal to the relative  $R_2$  resolution ( $R_{2\Delta\%}^p$ ) which is defined in a similar way:

$$D_{\Delta\%}^p = \sqrt{2} \cdot k_p \frac{\sigma_D}{(D_{max} - D_{min})} = \sqrt{2} \cdot k_p \frac{\sigma_{R2}}{(R_{2max} - R_{2min})} = R_{2\Delta\%}^p \quad (3)$$

As mentioned earlier, the here defined dose-resolution does not include stochastic variations in chemical concentrations, in dose delivery or in the calibration procedure. For that reason, dose-resolution can be considered as an intrinsic lower limit of type A uncertainty.

It should be emphasized that the dose-resolution is not only related to the type of gel dosimeter but also to the scanning protocol [26,27]. In some publications, the concept of dose resolution has been used as the criteria to compare different types of gel dosimeters. This may be misleading as these studies report on dose resolutions obtained with sub-optimal scanning parameters. The concept of dose resolution however is very practical to optimize the intrinsic NMR sequence in terms of intrinsic precision [27]. In optimizing the NMR sequence, it is also important to take into account the number of slices that are required for the 3D dosimetry application as the optimization is also dependent on the number of slices.

Depending on the available scanning facilities three different optimization strategies can be followed:

1. *Only a single spin-echo sequence is available:* It can be shown that if one has only a single spin-echo sequence a two-points method is preferred. In the two-points method, two differently  $T_2$ -weighted base images are acquired and the  $R_2$  is derived algebraically from the signal intensity in the two images according to the equation:

$$R_2 = \frac{\ln S_1 - \ln S_2}{TE_2 - TE_1} \quad (4)$$

with  $S_i$  and  $TE_i$  the signal intensity and the echo time in image  $i$  respectively.

The relative dose resolution is then given by:

$$D_{\Delta\%}^p \cong \frac{\sqrt{2}k_p}{SNR_1 \cdot \Delta TE \cdot (R_{2,max} - R_{2,min})} \sqrt{\frac{1}{N_1 + N_2} \cdot \left( \frac{e^{2R_2\Delta TE}}{1 - \psi_N} + \frac{1}{\psi_N} \right)} \quad (5)$$

$SNR_1$  is the signal-to-noise ratio in the first base image which is the image recorded with echo time  $TE_1$ . The echo time spacing  $\Delta TE = TE_2 - TE_1$ . Equation 5 also applies to the case where more acquisitions are taken in each image. The acquisition fraction is  $\psi_N = \frac{N_1}{N_1 + N_2}$  with  $N_1$  the number of acquisitions (averages) of the first image (with  $TE_1$ ) and  $N_2$  the number of acquisitions (averages) of the second image (with  $TE_2$ ). An optimal echo time spacing and acquisition fraction can be derived for a gel with  $R_2$  values in a range  $[R_{2,min}, R_{2,max}]$ . Tables 1 and 2 in publication [27] give the optimal echo time spacing and the optimal acquisition fraction for the two-points method.

2. *A multiple spin-echo sequence is available with a fixed number of echoes:* To acquire quantitative  $R_2$  images, a multiple spin-echo sequence is highly preferred above a single spin-echo sequence because several differently  $T_2$ -weighted images are acquired within the same measurement time increasing the overall signal-to-noise ratio in the  $R_2$ -images. The quantitative  $R_2$ -image is then obtained by fitting a mono-exponential decay-function to the pixel intensities of corresponding pixels. On many scanners, a multiple spin-echo sequence is available on the scanner. Very often, the number of available echoes is ‘hardcoded’ in the sequence. In that case, it is advisable to optimize the echo time interval. The echo time interval is defined as the time interval between the first and the last echo in the multiple spin-echo acquisition window. The optimal echo time interval can be derived from a graph provided in figure 9 of reference [26]. It is also found that the optimization also depends on the fitting algorithm that is used to derive the  $R_2$  value. For more than 7 echoes and using a  $\chi^2$ -minimization fitting algorithm, the optimal echo time interval is approximately 2 times the  $T_2$  value of the sample. To a good approximation this also applies to the median  $R_2$  for a phantom containing a range of  $R_2$  values.

3. *A multiple spin-echo sequence is available with an arbitrary number of echoes:* This is the most optimal situation from the perspective of optimization of the dosimetric precision when more slices are acquired. The reasoning behind this is based on the fact that within an optimal echo time recording period it is preferable to acquire as many echoes as possible. To optimise this sequence, the echo time spacing is taken as short as possible without introducing any artefacts. Then the number of echoes is optimized. Most often, there is an upper threshold on the available echoes in the multiple spin-echo sequence. When the recommended (optimal) number of echoes exceeds the number of available echoes, the echo time spacing is increased to cover the optimal echo time interval. In publication [27], table 5 gives the optimal number of echoes for a gel with  $R_2$  values in a range [ $R_{2\min}$ ,  $R_{2\max}$ ]. The number of echoes is limited by the minimal inter-echo-time-spacing which is determined by machine related characteristics such as maximum gradient strength, sampling rate and SAR considerations. In practice, it is also advisable to check for imaging artifacts (uniformity, dose errors and geometrical distortions) while decreasing the inter-echo-time-spacing.

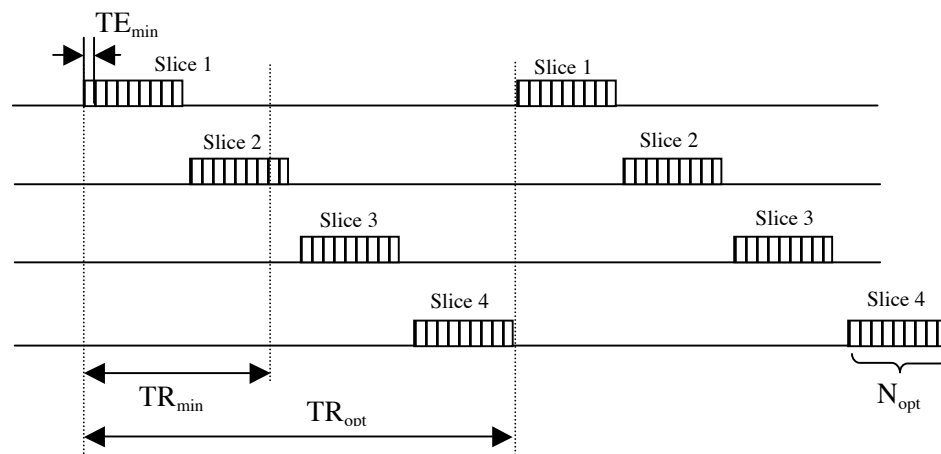


**Figure 3.** Multi-slice multi-echo sequence showing the optimal sequence parameters. The number of spin-echoes acquired for each slice is optimized.

Then, if more than one slice is acquired, the time interval between the end of the echo-time recording period and the repetition time can be used to scan another slice (figure 3). As from a certain number of slices, not all slices can be recorded within one repetition time. In that case, the repetition time can be extended to cover exactly the time needed to acquire all slices. The algorithm to determine the optimal echo time is described in [27].

### 3. Reproducibility study

#### 3.1. Materials and Methods

In previous studies, the fundamental radiation properties of several gel dosimeters were studied and it was found that PAGAT gel dosimeters demonstrated the least dose rate and temperature dependence during irradiation [23,24] and dependence on cooling rate [6]. Therefore, we chose to use PAGAT gel dosimeters in this reproducibility study. The polymer gel dosimeter was fabricated according to a procedure as described elsewhere [23]. Both an intra-batch and inter-batch reproducibility study were performed (figure 4). In the intra-batch reproducibility study, a large quantity of polymer gel was fabricated and poured in eight spherical borosilicate flasks (250 ml each) and nineteen test tubes (calibration vials). In the inter-batch reproducibility study, a complete gel dosimetry experiment was performed eight times in which each time 0.6 l of gel was fabricated and poured in a spherical 250 ml borosilicate flask and corresponding nineteen test tubes. In both experimental designs, each of the

eight spherical gel dosimeter phantoms was scanned together with its corresponding set of calibration vials.

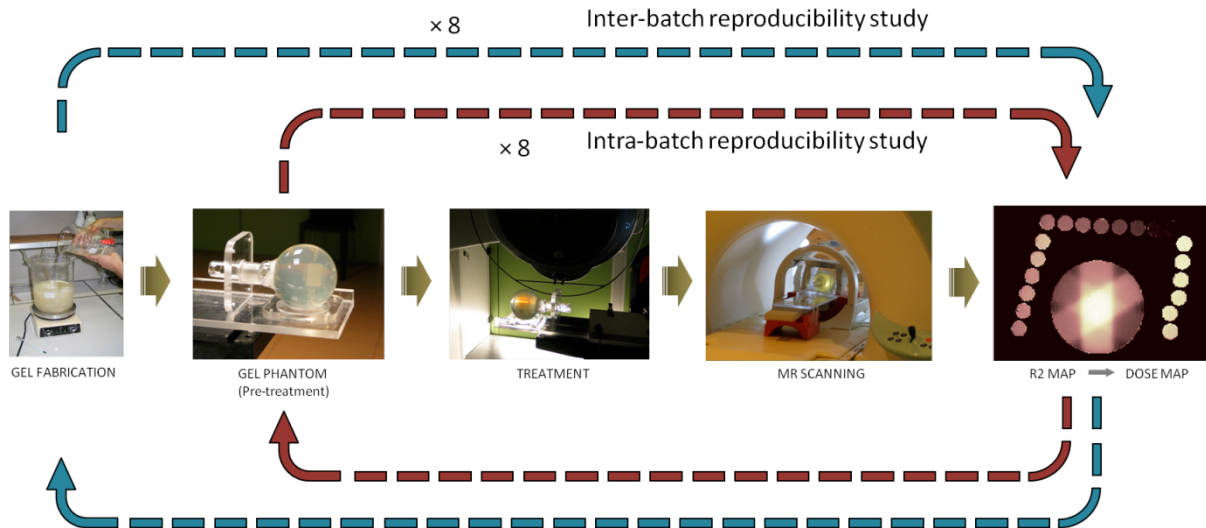


**Figure 4.** Inter- and Intra-batch reproducibility study of a gel dosimetry experiment.

After filling the recipients, the phantoms were stored in a large water reservoir (60 l) in order to ensure a similar temperature course in both the spherical phantoms and the calibration vials. A dedicated holder in PMMA was constructed to fixate the spherical phantoms during CT scanning, irradiation and MRI. CT images were taken from a spherical phantom which were transferred to the planning computer and a three beam coplanar irradiation was simulated using the treatment planning system Pinnacle™.

The irradiation treatment consisted of three coplanar beams with gantry angle at 180° (525 MU), 60° (150 MU) and -60° (375 MU) respectively. The calibration phantoms (test tubes) were irradiated at reference depth with a 10 cm × 10 cm photon beam at a variety of radiation doses to cover the calibration range. A reference measurement was performed in the centre of a similar spherical phantom filled with gelatine using a small volume ionization chamber (PTW semiflex 31010) (figure 5). The measured dose in the centre of the spherical phantom amounted to 11.28 Gy, corresponding with a dose difference of 0.4 % with the TPS.

Quantitative NMR spin-spin relaxation rate ( $R_2$ ) maps were recorded from the spherical phantom surrounded by the corresponding calibration tubes with a 1.5 T MRI scanner (Avanto, Siemens) using a multiple spin-echo sequence with 32 echoes and echo spacing ( $\Delta TE$ ) 40 ms. The other scanning parameters were TR = 10 s, voxel size = 1 mm × 1 mm × 5 mm, receiver bandwidth (BW) = 130 Hz/pixel and 10 slices, resulting in a total scan time of approximately 50 minutes.  $R_2$  maps were constructed from 31 base images (ignoring the first base image) using a  $\chi^2$ -minimization algorithm [26,27]. All gel dosimeter phantoms were scanned at different instances: 6h, 30h, 54h and 92h post-irradiation in the intra-batch reproducibility study and at 19h, 43h and 85h post-irradiation in the inter-batch reproducibility study. A detailed description of the full reproducibility study can be found in a publication which is currently in press [28].

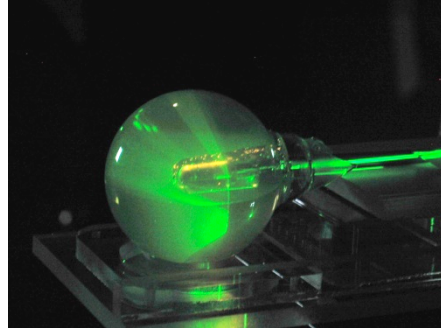


**Figure 5.** Reference measurement with an ionization chamber in the centre of the spherical phantom.

### 3.2. Results and discussion

The dose distributions and deviations with respect to the TPS planned dose distribution (and ionization chamber) after calibration with their corresponding set of calibration vials were found to be very similar. Gel measured dose maps from the eight phantoms of the inter-batch reproducibility study are shown in figure 6. Although the dose maps look very similar, deviations become more apparent from dose profiles in comparison with a dose profile through the TPS (figure 7).

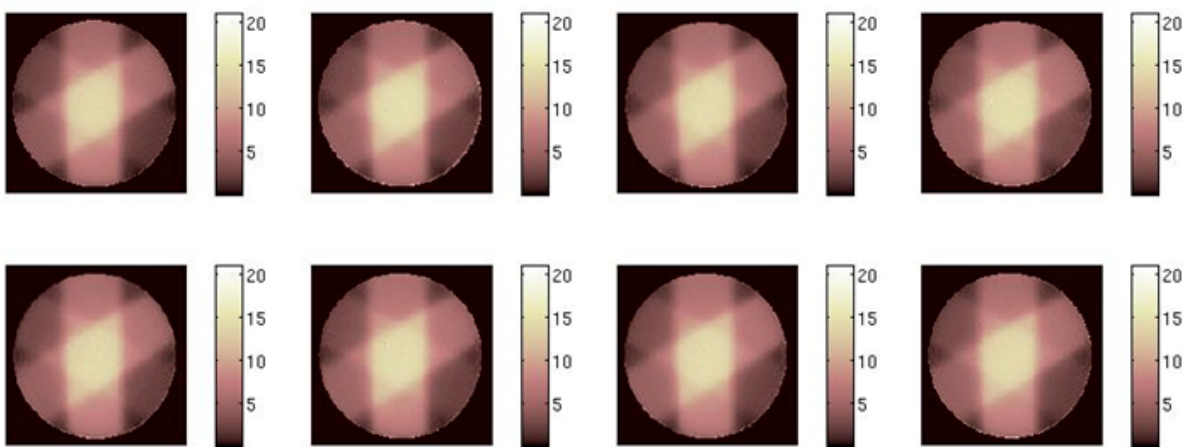


**Figure 6.** Gel measured dose maps through the isocentre of the eight different gel dosimeters of the inter-batch reproducibility study. The colour scale is in Gy.

Variations in  $R_2$  in the order of 8% occur between the different gel dosimeters in the inter-batch reproducibility study (figure 7c). However, using the appropriate corresponding calibration curve for each gel dosimeter phantom, the actual average dose deviation between the different gel dosimeters is reduced to less than 3%. However, in a few cases at other scan times, larger deviations (in the order of 10%) were found for the same phantoms and a deviation with the ion chamber measured dose (and TPS calculated dose) of more than 10% is also apparent from figure 7d. The fact that a good precision was found in some scan sessions but not in all is indicative of an error source that changes after irradiation. It was later found that the major source of the irreproducible systematic dose error was attributed to changes in temperature during scanning between calibration vials and volumetric gel dosimeter phantoms (see section 4) that can be solved by the aid of active temperature stabilization in the MRI scanner (see section 5). It is obvious that by use of a renormalization using two internal dose points (in a low dose and high dose region) the measured dose distributions are matched (figure 7e). This renormalization procedure or relative scaling has been applied by most research groups. With this renormalized dose distribution, more than 97% of all points of the measured dose distribution fulfilled the gamma-criterion of 3% / 3mm.

Although in the intra-batch reproducibility study (results not shown), a better match was found in the initial  $R_2$  distribution, the systematic and random dose errors were found to show a similar behaviour as these found in the inter-batch reproducibility study.

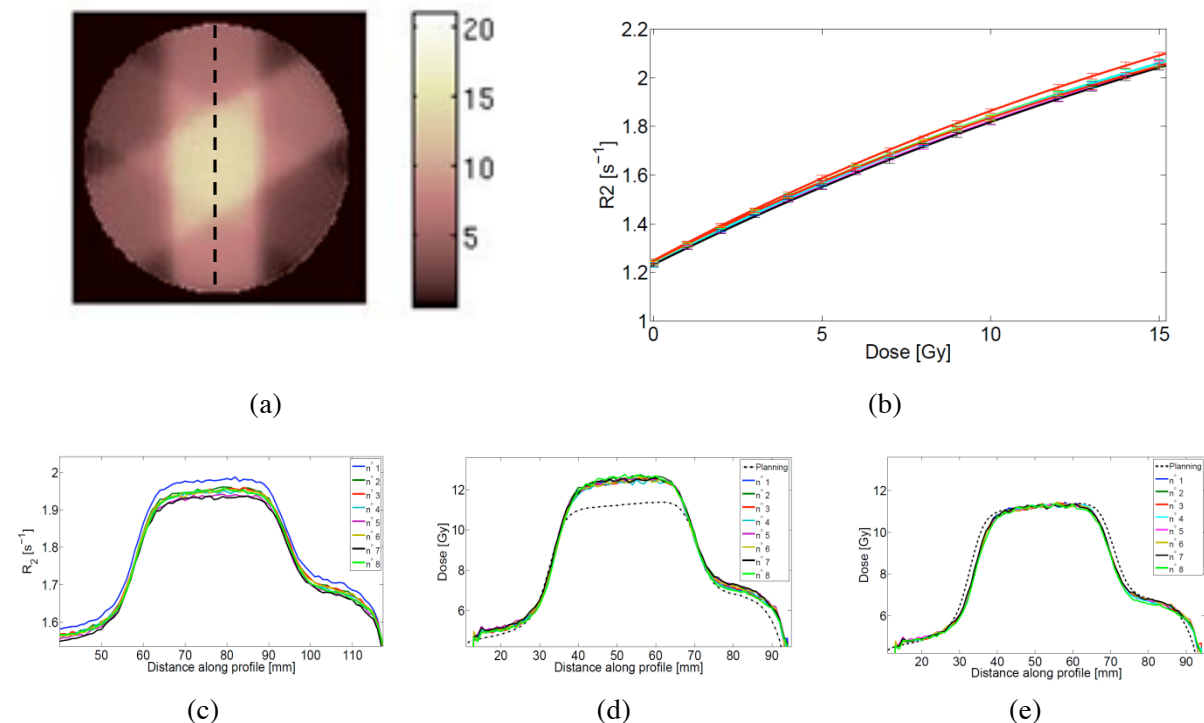


**Figure 7.** Dose map of one of the eight phantoms of the inter-batch reproducibility study (a) indicating the location of intensity profiles as shown in (c) - (e) for all eight phantoms. The corresponding dose- $R_2$  response curves for all eight phantoms are shown in (b).  $R_2$  profiles demonstrate some variation which after calibration with their corresponding dose- $R_2$  calibration curves (b) disappear. However, a significant systematic deviation with the TPS planning profile (dotted line) remains. By applying a renormalization of the dose- $R_2$  calibration ('relative' internal calibration) the dose profiles match.

From this study, it was concluded that polymer gel dosimetry for these small sized volumetric gel dosimeter phantoms can be performed with a high dosimetric precision and accuracy by applying a renormalization of independent dose measurements using two internal reference points. In the verification of a treatment plan with gel dosimetry, it is necessary to verify the absolute dose in the reference points by use of an independent dosimetric point-measurement (ion chamber). For realistically sized humanoid shaped phantoms with volumes of more than 2 litre, a renormalization may not be sufficient because of internal temperature differences within the volumetric gel dosimeter phantom.

To assess the effect of various error sources on the dose reading, it is illustrative to consider the dose sensitivity. The dose sensitivity of a PAGAT gel dosimeter is in the order of  $0.06 \text{ s}^{-1} \cdot \text{Gy}^{-1}$  (see figure 7b). With a realistic dose range of 15 Gy, a dose error of 1% with respect to the measured dose range amounts to 0.15 Gy or only  $9 \cdot 10^{-3} \text{ s}^{-1}$ . This places great demands on the accuracy and precision by which  $R_2$  is measured.

#### 4. Physico-chemical origins of dose error in polymer gel dosimeters

##### 4.1. Gel fabrication and storage temperature

The influence of the temperature history during the storage period between fabrication and irradiation storage of the gel dosimeter on the dose response curve has been assessed for both PAGAT and MAGAT gel dosimeters [6]. After fabrication, different calibration phantoms were subjected to different temperature trajectories that are realistically encountered during cooling a gel in a refrigerator. The temperature trajectories were measured by use of fibre optic probes. It was found that the dose- $R_2$  response of MAGAT gel dosimeters was significantly more dependent on the storage temperature than that of PAGAT gel dosimeters.

To investigate the effect of a temperature gradient in a volumetric phantom after fabrication and before irradiation, a box-shaped Barex™ recipient was filled with PAGAT gel and a temperature gradient was induced in the phantom for 14 hours by exposing opposite sides of the phantom to different temperatures ( $5^\circ\text{C}$  and  $25^\circ\text{C}$  respectively). The temperature gradient was measured by use of fibre optic temperature probes that were inserted in a similar blank phantom and in a similar experiment. More findings are detailed in a recent publication [29].

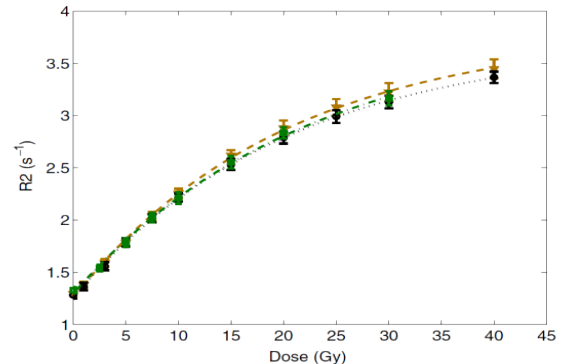


**Figure 8.** Dose- $R_2$  response plots of PAGAT gel dosimeters cooled down with different temperature courses [6].

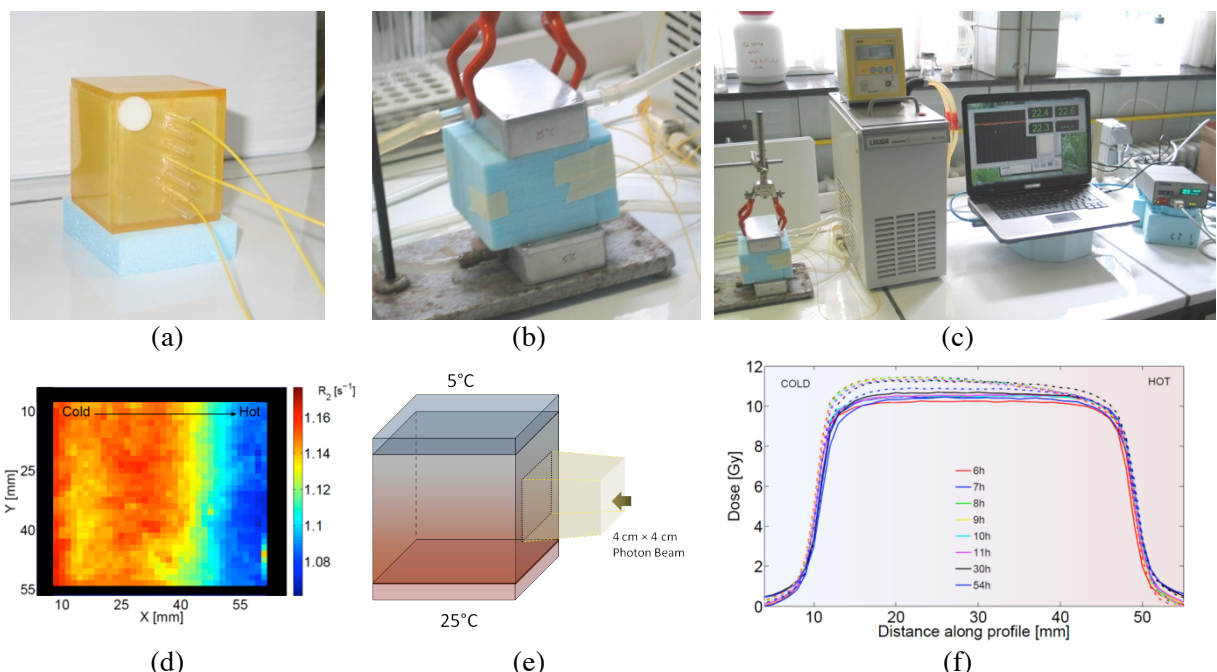


**Figure 9.** Experiment that illustrates the effects of temperature differences during storage (i.e. between fabrication and irradiation) on the measured dose distribution. A box-shaped gel phantom (a) is exposed to a temperature gradient during 14 hours before irradiation (b-c). An  $R_2$  map of an unirradiated phantom shows a variation of  $0.07 \text{ s}^{-1}$  in the direction of the gradient (d). A phantom that is irradiated at a lateral side with a square beam also shows a negative dose gradient in the direction of the temperature gradient.

The  $R_2$  of an unirradiated gel phantom that was exposed to a temperature gradient shows a negative non-linear response with increasing temperature (figure 9d). A dose overestimation is also found at the cold side of the phantom. However, this over-response decreases with time post-irradiation (figure 9f).

#### 4.2. Irradiation temperature dependent dose- $R_2$ response

It was found that in some polymer gel dosimeters the temperature during irradiation has an influence on the dose-response [23]. This is likely due to a temperature dependent change in the diffusivity of the monomers in the gel matrix and a change in the chemical reaction kinetics. It is mainly the dose- $R_2$  sensitivity that is influenced by the temperature increase. The intercept is not affected (figure 10). The dependence on temperature during irradiation has also raised concerns on the influence of the reaction heat that is released during the exothermal radiation induced polymerization reaction [30].

In large volumetric phantoms, the temperature increase upon irradiation is not uniformly distributed within the phantom as a result of the non-uniform dose distribution. Moreover, after treatment the temperature course in a large volumetric phantom is also spatially non-uniform and depends on both the initial dose distribution and on the thermal characteristics of the phantom and boundaries. As a result, dose read errors may be expected. To investigate the effect of momentary temperature increases on the measured dose- $R_2$  response, calibration vials were irradiated under different imposed temperature trajectories [29].

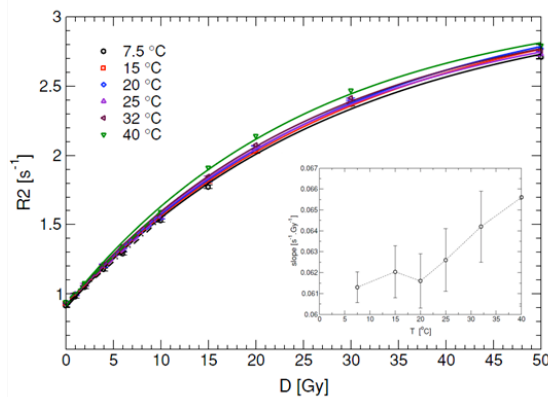
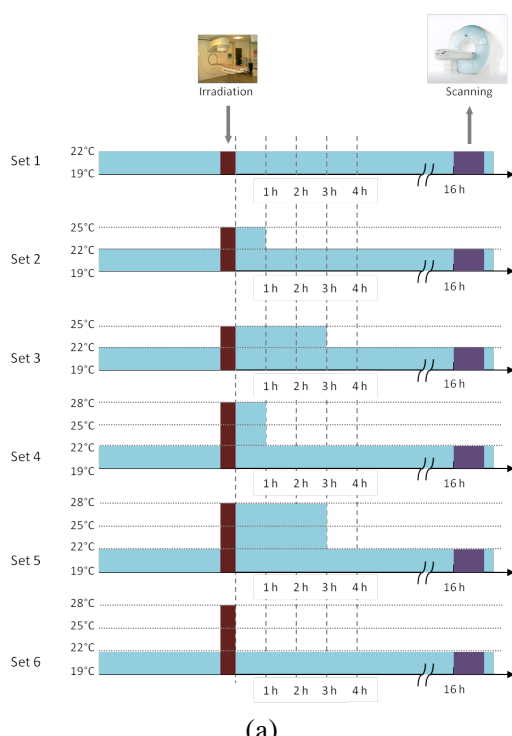
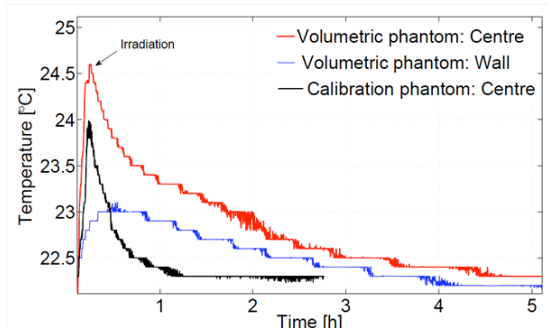


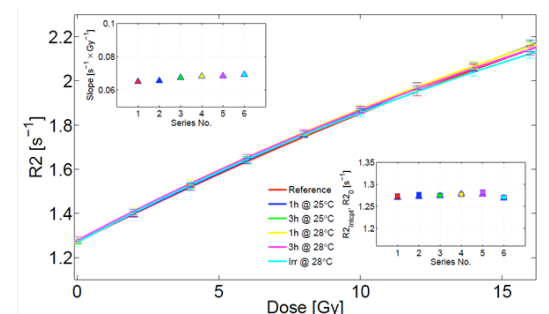
**Figure 10.** Dependence of the dose- $R_2$  response on the temperature during irradiation. The inset shows the corresponding slope as a function of irradiation temperature [6].



(a)



(b)



(c)

**Figure 11.** Imposed temperature course on 6 different sets of calibration tubes (a) that mimic extreme conditions of exothermal heating at different locations in a volumetric phantom (b). The dose- $R_2$  response curves of the six different sets are plotted in (c).

No significant effect of temperature changes during and immediately following irradiation could be detected (figure 11).

#### 4.3. Chemical instabilities

Two kinds of chemical instabilities have been observed in polymer gel dosimeters [6, 31]. One affects the slope of the dose– $R_2$  response plot and is related to post-irradiation polymerization of the comonomer/polymer aggregates. It is observed that post-irradiation polymerization in a PAGAT gel dosimeter only lasts 12 hours after irradiation (figure 12b). The other instability affects the intercept of the dose– $R_2$  plot (figure 12c), lasts for up to 30 days and is related to the gelation process of gelatine. These mechanisms have later been confirmed through FT-Raman spectroscopy [32]. The chemical instability depends strongly on the polymer gel composition [6]. In order to minimize systematic errors it is advisable to scan the gel dosimeter phantom together with the corresponding calibration vials.

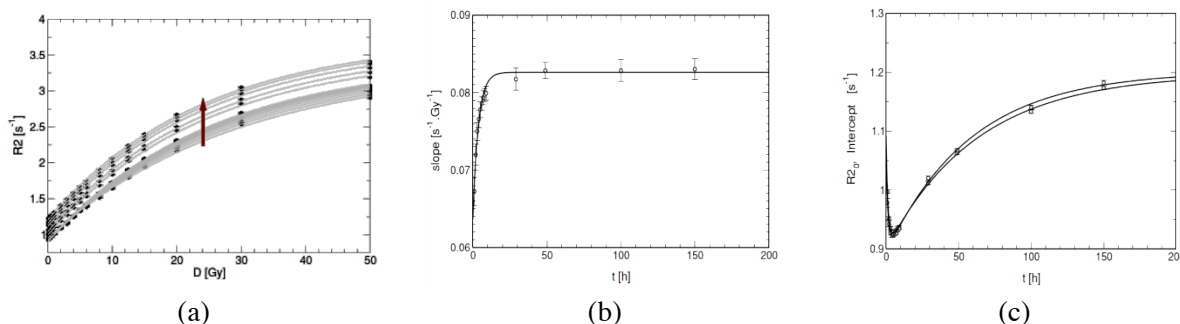


**Figure 12.** Dose– $R_2$  plots of a PAGAT gel dosimeter recorded at different post-irradiation times (a) and corresponding changes in slope (b) and intercept (c) [23].

#### 4.4. Loss of spatial integrity

Loss of spatial integrity is a consequence of the diffusion of the active components or oxygen in the gel dosimeter. An extreme case is the Fricke gel in which the diffusion of ferric and ferrous ions results in a blurring of the measured dose distribution over time [33–35]. But also in polymer gel dosimeters can the diffusion of monomers at very high dose gradients during irradiation [36] and in the first hours after irradiation [25] have an influence on the measured dose distribution. Unreacted monomer diffusing from unirradiated region may react with large polymer radicals in the irradiated region in the first hours after irradiation. A quantitative model is presented that links the loss of spatial integrity with the monomer diffusion and post-irradiation polymerization [37].

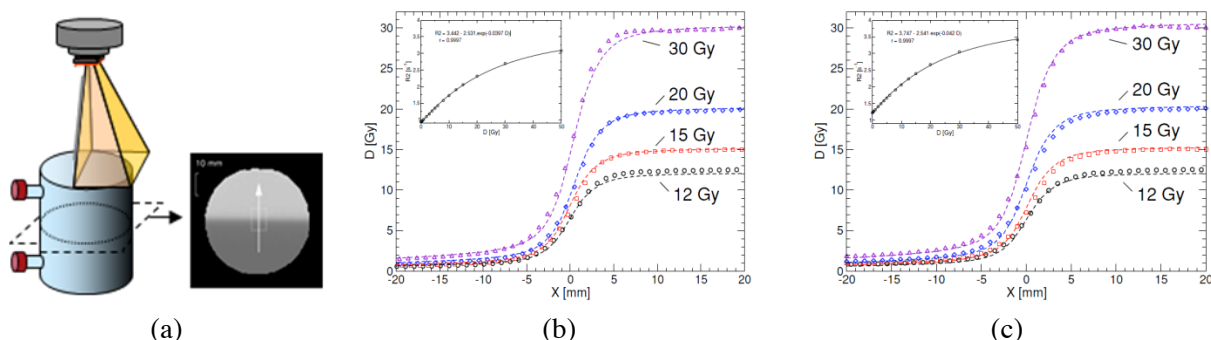


**Figure 13.** Dose penumbra at the edge of a half-blocked 10 cm × 10 cm square photon beam (a) measured with a PAGAT gel dosimeter acquired 10 hours post-irradiation (b) and 6 days post-irradiation (c).

No measured dose overestimation are found in PAGAT gel dosimeters for doses below 20 Gy (figure 13) while for MAGAT gel dosimeters dose overestimations have been seen near the penumbra region for doses of 10 Gy [23].

#### 4.5. Dose rate dependent dose- $R_2$ response

As radiation induced polymerization reactions are regulated by complex reaction schemes involving initiation, propagation, cyclization, transfer and termination [38], it is not surprising that the dose- $R_2$  response of polymer gel dosimeters is dependent on dose rate [23]. Moreover, some reaction pathways are also diffusion controlled. The same mechanism is at the origin of the LET dependence of polymer gel dosimeters [39]. It has been found that this effect is more pronounced in MAGAT gel dosimeter as compared to PAGAT gel dosimeters [26] (figure 14). The influence of the dose rate dependent dose- $R_2$  response on the accuracy of dose verification with PGD should not be underestimated as it may lead to a depth dependent dose-response. A dose-rate dependency may be detrimental for a dosimeter. Nevertheless, the dose-rate dependence has not been documented for all gel dosimeter systems.

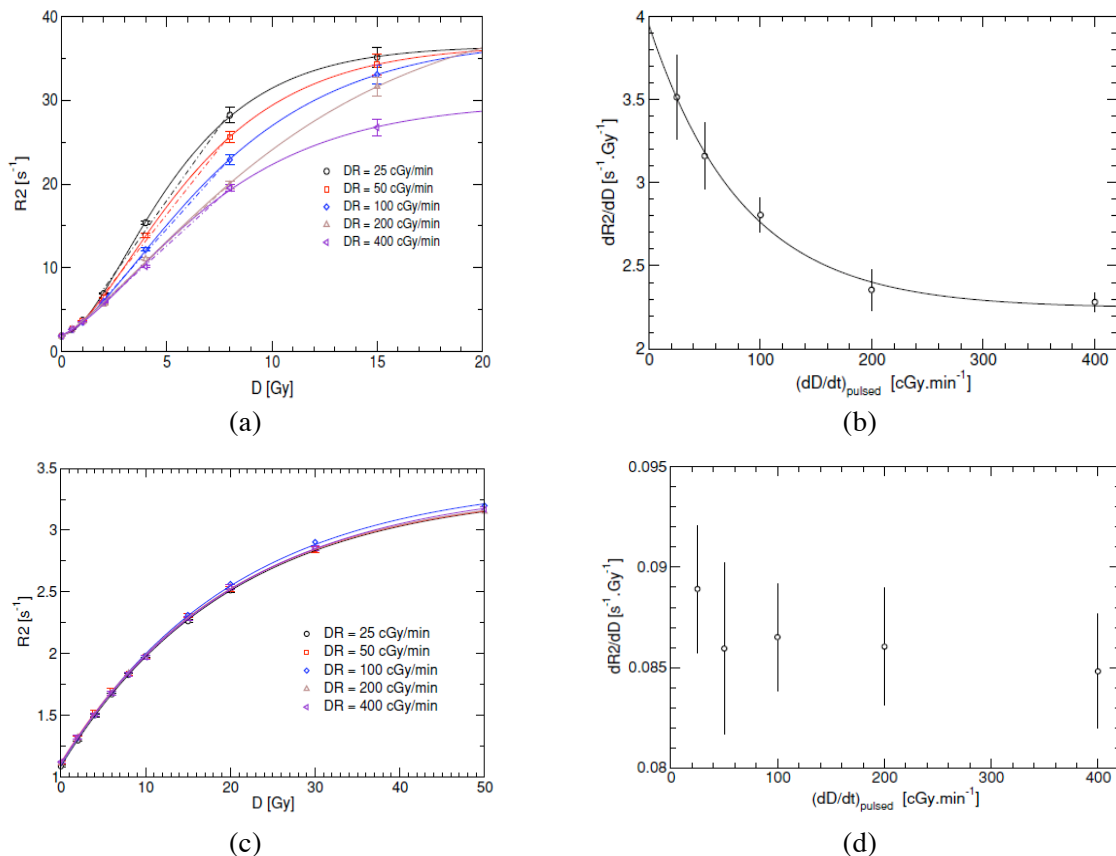


**Figure 14.** Dose- $R_2$  response curves for different dose rates for MAGAT (a) and PAGAT (c) gel dosimeters. The corresponding change in dose sensitivity of both gel dosimeters is recorded in (b) and (d) respectively.

#### 4.6. Oxygen effects

With the introduction of 'normoxic' polymer gel dosimeters [40], using an anti-oxidant to scavenge oxygen from the gel, it was expected that problems related to oxygen infiltration in the gel would be solved [41]. Although the procedure of fabrication has been significantly simplified, the issue of oxygen infiltration after closing the dosimeter is still present [8,42]. This also restricts the use of different cast materials and restricts the storage time before irradiation [42] (figure 15). In PAGAT gel dosimeters a reduced dose- $R_2$  sensitivity is also found for increasing amounts of anti-oxidant [42].

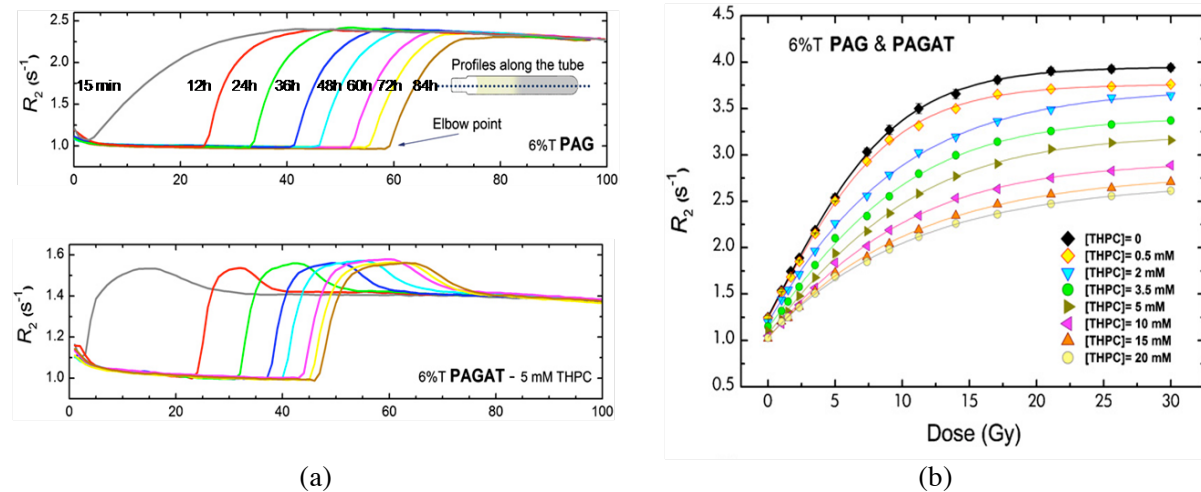


**Figure 15.** Infiltration of oxygen from the top of the test tube (left to right) after irradiation in PAG and PAGAT gel dosimeters. Test tube samples have been irradiated to a dose of 5 Gy after the times indicated (a). The dose sensitivity of PAGAT gel dosimeters also depends on the amount of THPC. Adopted from Sedaghat et al [42].

Also, the effect of oxygen infiltration after irradiation has been investigated. No significant effect was detected for an oxygen redistribution 48 hours post-irradiation [29].

It is concluded that even with normoxic polymer gel dosimeters, cast materials should still be conscientiously chosen with Barex™ and glass as the optimal choice until now. The antioxidant should be well mixed in the gel and infiltration of oxygen from the inlet of the recipient should be avoided. No significant post-irradiation effect of oxygen could be established.

### 3.7. Recipient wall-effects

To avoid permeation of oxygen through the recipients wall, Barex® or glass are often used as phantom materials. It should be noted that some glass may contain heavy metals. These specific glass materials may result in a stronger attenuation of the incident beam and may also result in beam hardening. Some caution is therefore advised in selecting glass as cast materials.

It was shown by Monte Carlo simulations that the effect of a borosilicate glass wall and backscatter of a layer of air did not have a significant effect on the delivered dose in a test vial [43].

As differences in dose-R2 response were observed independently by many investigators, an experiment was designed in which a test tube was inserted in a volumetric phantom (figure 16).

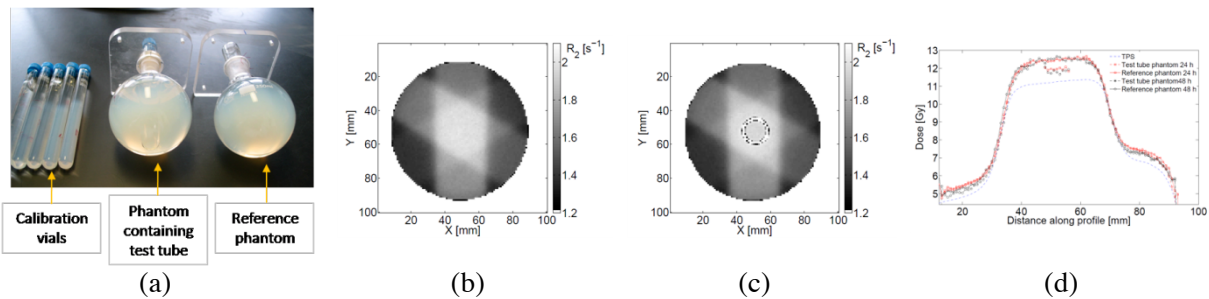


**Figure 16.** Experiment in which a test tube with gel was inserted in a larger volumetric phantom (a). A small under response (c,d) was observed in the test tube as with respect to a reference phantom (b) which was attributed to a temperature difference during scanning of 0.3 °C.

A small difference in dose response was observed in the test tube as compared to a reference phantom. The observed effect has been found to be not reproducible and has been attributed to small temperature differences during scanning between the gel in the test tube and outside the tube in the volumetric phantom. All other MRI related effects including magnetic susceptibility differences,  $B_1$  field inhomogeneities were excluded as possible explanations for the observed effect by additional measurements of the  $B_0$  and  $B_1$  magnetic field. Also the effect of the glass tube on the irradiation beam was excluded by independent pinpoint ion chamber measurements in the tube-containing and reference phantom. Repeated readouts with MRI demonstrated that the effect was also irreproducible in both an irradiated and a blank phantom.

## 5. Readout related sources of dose uncertainty in polymer gel dosimeters

Whatever imaging technique is applied to map a dose-effective contrast ( $R_1$ ,  $R_2$ , MT, optical density, X-ray absorbance, ultrasound attenuation, dielectric constant, etc.) there are two essential criteria that should be accomplished in the imaging technique: First of all, the images should be accurate both in space as in dose (i.e. not contain systematic errors) and secondly, the stochastic deviations on each voxel should be as low as possible within a reasonable measurement time and for a certain image resolution. An interesting parameter to evaluate the stochastic deviations is the minimum detectable dose difference, defined as the dose resolution [44].

Imaging artefacts may compromise the dose accuracy in each voxel and can deform the image causing a spatial inaccuracy. Dosimetric imaging artefacts can be machine-related or object-related. Machine-related artefacts originate from imperfections in the scanning device while object-related artefacts originate from the dosimeter itself.

**Table 2.** Overview of important artifacts that may occur in MRI gel dosimetry classified by two criteria. The abbreviation as most often used in the literature is also given.

| Geometrical distortions                               |   | Dose inaccuracies                                     |   |
|---|---|---|---|
| Machine related                                       | Object related                                    | Machine related                                       | Object related  |
| $B_0$ Field non-uniformity<br>$B_0(x,y,z)$            | Susceptibility differences<br>$\Delta\chi(x,y,z)$ | Eddy currents<br>$\Delta B_0(t), \Delta g_{x,y,z}(t)$ | Temperature drift<br>$T(t)$                           |
| Gradient non-linearity<br>$g(x,y,z)$                  | Chemical shifts<br>$\sigma(x,y,z)$                | Stimulated echoes<br>$M_{xy}(TE)$                     | Molecular self-diffusion<br>$D(x,y,z)$                |
| Eddy currents<br>$\Delta B_0(t), \Delta g_{x,y,z}(t)$ |   | $B_1$ field non-uniformity<br>$B_1(x,y,z)$            | Standing waves and dielectric effects<br>$B_1(x,y,z)$ |
|   |   | Slice profile<br>$M_{xy}(z)$                          | Susceptibility differences<br>$\Delta\chi(x,y,z)$     |

The most-important machine-related MRI artefacts are attributed to eddy currents, stimulated echoes,  $B_1$  field inhomogeneity, imperfect slice profiles and standing waves. These machine-related artefacts may depend on the gel dosimeter shape and make it difficult to make general statements on the accuracy of the dosimeter. A larger phantom or a phantom with sharp edges may perform differently than a smaller cylindrical or spherical shaped phantom. Standing-waves can severely deteriorate the dose distribution in dosimeters with specific shapes and spatial dimensions but may be almost completely absent if the dosimeter phantom has a slightly different shape.

Object-related MRI artefacts are mainly attributed to a temperature drift during scanning or molecular self-diffusion. For a more detailed overview of different MRI artefacts and compensation strategies we refer also to previous communications [45,46].

In optical imaging, dosimetric artefacts are related to reflection and absorption by the recipient walls, off-axis positioning of the recipient, variation of the laser output and photo-detector and light-scattering by both impurities in the matching fluid, container and by the polymer [47-50].

#### 4.1. Machine-related geometrical distortions

**4.1.1.  $B_0$  magnetic field inhomogeneities.** Geometrical distortions may originate from a non-uniform magnetic field of the MR scanner. Important to note is that displacements and scaling of the whole phantom may occur both in the image plane as out of the image plane. The extend of the distortion is also dependent on the receive (pixel) bandwidth. The pixel bandwidth is inversely related to the readout time of each echo (frequency encoding window) in the pulse sequence. A shorter spin echo readout time will result in a larger pixel bandwidth and corresponding smaller distortion for a similar magnetic field non-uniformity. However this will go at the cost of signal-to-noise ratio, hence dose resolution. The magnetic field of the scanner is generally expressed by the manufacturer in parts-per-million (ppm) of the main magnetic field within a certain volume-of-interest. The displacement of a pixel can be easily calculated from equation 1:

$$\Delta x = \frac{\gamma \cdot \Delta B_0}{2\pi \cdot BW_{pix}} \cdot \left( \frac{FOV_x}{N_x} \right) \quad (6)$$

where  $\Delta x$  is the shift in the frequency encoding direction in metric units,  $\gamma$  is the gyromagnetic constant ( $\gamma = 2.6753 \cdot 10^8 \text{ s}^{-1} \text{ T}^{-1}$ ),  $\Delta B_0$  is the magnetic field inhomogeneity,  $BW_{pix}$  is the bandwidth per pixel ( $BW_{pix} = 1/T_{ro}$ ),  $FOV_x$  is the field-of-view in the frequency encoding direction and  $N_x$  is the number of pixels in the frequency encoding direction. As an example, a 1 ppm field deviation on a 3T MRI scanner corresponds to a field inhomogeneity  $\Delta B_0 = 3 \mu\text{T}$  which results in a shift of approximately one pixel for a bandwidth per pixel of  $BW_{pix} = 130 \text{ Hz}$  ( $T_{ro} \cong 8 \text{ ms}$ ). Note that a higher spatial resolution (smaller pixel size:  $\left( \frac{FOV_x}{N_x} \right) \downarrow$ ) will result in a smaller spatial shift in metric units.

Similarly, a shift in the phase encoding direction in pixel units is given by

$$\Delta y = \frac{\gamma}{2\pi} \cdot \Delta B_0 \cdot t_{ph} \cdot \left( \frac{FOV_y}{N_y} \right) \quad (7)$$

where  $t_{ph}$  is the duration of the phase encoding gradient,  $FOV_y$  is the field-of-view in the phase encoding direction and  $N_y$  is the number of pixels in the phase encoding direction. The time of the phase encoding gradient is usually significantly smaller than the readout time (in the order of 1 ms) and the distortion can therefore be ignored in standard MRI sequences (in the case of  $R_2$  mapping: a multiple spin-echo sequence). However, in the case of echo-planar imaging, the shift in phase-encoding direction is given by

$$\Delta y = \frac{\gamma}{2\pi} \cdot \Delta B_0 \cdot t_{esp} \cdot FOV_y \quad (8)$$

where  $t_{esp}$  is the time between subsequent echoes (e.g. 1 ms) and  $FOV_y$  the field-of-view in the phase-encoding direction. For the same field homogeneity ( $\Delta B_0 = 3 \mu\text{T}$ ) and a field-of-view of 250 mm, this would result in an image distortion of more than 3 cm !

The shift in the slice selective direction is given by:

$$\Delta z = \frac{\Delta B_0}{G_z} \quad (9)$$

where  $G_z$  is the gradient strength of the slice selective imaging gradient. For the above example with a magnetic field inhomogeneity of 1 ppm and a slice selective magnetic field gradient strength of  $G_z = 3 \text{ mT/m}$  the slice shift will also be 1 mm. Note that in the equations above the shifts and indices are taking in an orthogonal system of reference (i.e. x,y,z). Note that MRI allows the acquisition of oblique slices where the same equations apply but with the indices x,y,z replaced by the new coordinates.

To measure the magnitude of deformations from non-linear gradients and main magnetic field inhomogeneities several phantoms have been proposed [51-53]. In observing in-plane distortions a pin-cushion phantom is often used. To account for errors in the construction of the phantom, the phantom is first scanned by use of CT. By overlaying the images indicating the positions of the tubes of the MR images on the CT images a distortion map can be derived.

External (fiducial) markers on the phantom can also be used to allow image fusion with computer planning or other dosimetry techniques. These external markers may give a first indication of deformations or slice displacements. It is important to adequately chose the fiducial markers in order not to cause any misreading as a result of susceptibility differences or chemical shifts of the fiducial markers themselves. A scaling error of the phantom can also be detected by use image fusion/matching software.

**4.1.2. Gradient non-linearity.** The imaging gradients are expected to be linear. However, this only applies to the central part of the scanner. Distortions can result from any non-linearity in the magnetic field gradients and can be expected at the outer edges of a phantom with dimensions large as compared to the scanner. These distortions can be described by an infinitesimal spatial approach of equations (6)-(9). A distortion correction method for magnetic field and gradient non-linearity has been proposed [54]. Another method to correct for local magnetic field distortions is by a technique called ‘view-angle-tilting’ [55]. This method has the advantage that no post-processing is needed but has the disadvantage that the point-spread function is broadened which may lead to an erroneous interpretation of the spatial resolution.

**4.1.3. Eddy currents.** Apart from static deviations in the magnetic field and gradients, the magnetic field may also deviate from the theoretical expected shape due to time-varying magnetic field components. These time-dependent magnetic field deviations are caused by ‘eddy currents’. The eddy currents are induced through switching of the imaging gradients giving way to an electromotive force that acts on the cryostat and metal casings. Several techniques to measure and analyze eddy currents in clinical scanners have been described [56-64]. The eddy current induced magnetic field is mostly described by a first order approximation composed of a global offset of the main magnetic field,  $\Delta B_0(t)$  and a change in the magnetic field gradients,  $\Delta g_i$  ( $i = x, y, z$ ) [57]. The eddy current related spatial encoding errors are mainly due to eddy current fields that are present during frequency

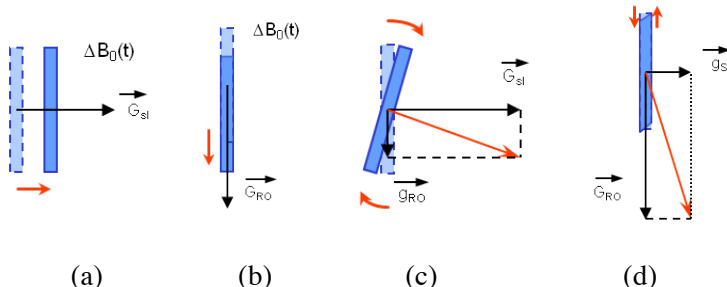


**Figure 17.** Different slice displacements caused by eddy currents invoked by switching of slice selection and frequency encoding gradient. An offset in the main magnetic field during slice selection causes a slice shift in the direction of the slice selective gradient (a) while a main magnetic field offset during frequency encoding causes a shift in the direction of the frequency encoding gradient (b). A gradient offset induced by eddy currents of the frequency encoding gradient will cause a slice rotation in the direction of the freq encoding gradient (c) while a gradient offset induced by the slice selective gradient will cause a change in viewing direction (d).

encoding and slice selection. Depending on the moment in the sequence that eddy currents are present, they will cause slice shifts or slice tilting in different directions (figure 17). To measure slice displacements, a pyramidal phantom can be used [56].

#### 4.2. Object related geometrical distortions

**4.2.1. Magnetic susceptibility differences.** In extending gel dosimetry to phantoms that include air cavities (for example to investigate effects of electronic disequilibrium), materials with different electron densities are inserted in the gel phantom. These materials very often have a different magnetic susceptibility ( $\chi$ ). This will result in susceptibility related distortions in the base images and in the final parametric images. Again, the distortion can be described with the equations (1)-(4). The distortions depend to a large extend on the position of the gel phantoms in the scanner. The magnetic field non-uniformity can be computed by numerically solving the Maxwell equations [65,66] or can be measured with MRI using a dedicated sequence [67]. Several compensation strategies have been developed to correct the image distortions [68-69]. An example of a susceptibility related artifact is shown in figure 18. This example was obtained by coincidence: In order to save some measurement time, two gel phantoms were placed in the scanner at the same time. The magnetic field and the frequency encoding direction are oriented upward in the images. It can be clearly seen that the phantoms are distorted near the interface between the phantoms. When the phantoms are oriented from left to right in the scanner the deformation disappears. Calculated magnetic field maps of both phantoms in an external magnetic field clearly demonstrate the much smaller field deviation when both phantoms are placed side-by-side perpendicular to the external magnetic field (figure 18c and d). Also changing the frequency and phase encoding direction will make the distortion disappear. Susceptibility induced deformations have been also observed when a guiding catheter for a brachy source is inserted inside a gel phantom [70]. In humanoid shaped phantoms, sharp boundaries may also result in susceptibility induced magnetic field distortions. These can be also compensated by placing the humanoid shaped phantom in a larger cylindrical recipient filled with paramagnetic contrast agent doped water. The contrast agent serves to lower the  $T_2$  value beyond the first echo time in the multiple spin echo sequence in order to compensate artifacts from turbulent flow in the container.

**4.2.2. Chemical shifts.** Also the inclusion of materials with a different chemical composition (organic liquids, fats) in the gel may result in a (chemical) shift of these objects in the frequency encoding direction.

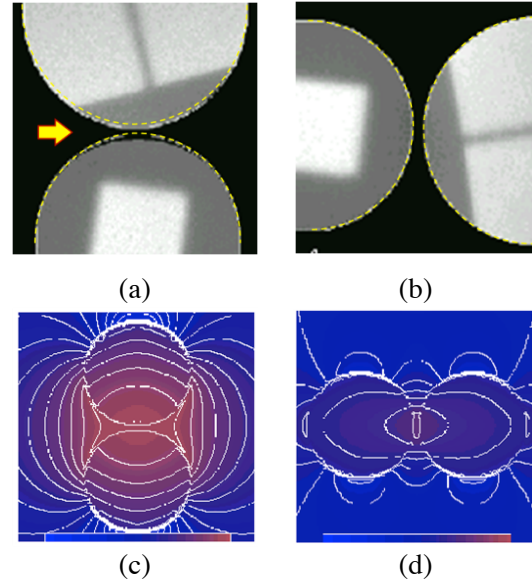


**Figure 18.** Two cylindrical gel phantoms positioned after each other in the direction of the external magnetic field of the scanner results in susceptibility related deformations (a) while if they are placed next to each other (b) no deformations are observed. The dashed lines are drawn on the image to show the actual boundary of the phantoms. Calculated magnetic field maps (c-d) demonstrate the significantly smaller effect in (b).

### 4.3. Machine-related dose inaccuracies

**4.3.1. Eddy-currents.** Eddy-currents may also invoke dose inaccuracies. The magnetic fields induced by eddy currents experience a certain decay time. The succession of many imaging gradients in a multiple spin-echo

sequence may lead to an increase in the magnetic field during the start of the sequence. This may lead to slice profile imperfections. It has been shown that eddy current effects can be minimized by playing out a gradient train before the start of the actual multi spin-echo acquisition [70]. This is attributed to a change in excitation history of stimulated echo-components. The result is a change in the measured  $T_2$ -decay curve. As the eddy currents (and especially the magnetic field offset) are dependent on the imaging direction, the disturbance of the excitation history of stimulated echoes is different and therefore also the measured  $R_2$  values (figure 19). Before setting up an actual gel dosimetry experiment, it is important to investigate a possible dependence of the acquired  $R_2$  values on imaging direction and other parameters. It is advisable to use a calibration plot that is derived from scans acquired with the same imaging parameters.

**4.3.2. Stimulated echoes.** Stimulated echoes may occur in a multiple spin-echo sequence as a result of imperfect (finite) excitation and refocusing pulses. The finite excitation and refocusing pulses result in excitation profiles that deviate from a rectangular profile (figure 20). As a result, the spin magnetization pathways vary along the slice encoding direction [56,71]. It is typically found in a multiple spin echo sequence that the signal intensity in the first two spin-echo base images deviate from the exponential decay curve. It is advisable to remove the first two base images from the fitting. The spin-echoes in a multiple spin-echo sequence are separated at equidistant time intervals for the same reason.

**4.3.3.  $B_1$  field non-uniformity.** Different RF coils can be used to scan the gel phantom dosimeter. However, coils should be chosen very carefully as the radiofrequency field of the coils is only uniform within a limited region. With receive/transmit coils, an imperfect excitation may occur outside the homogeneous region. As a result, the spin magnetization history in the multiple spin-echo sequence may deviate and stimulated echoes will be created [72]. When scanned with a CP transmit/receive head coil, the  $R_2$  map was found to be uniform only over an area of 120 cm in the centre of the coil, while the  $R_2$  values (apparent dose values) decreased considerably near the edges of the coil (figure 21a).

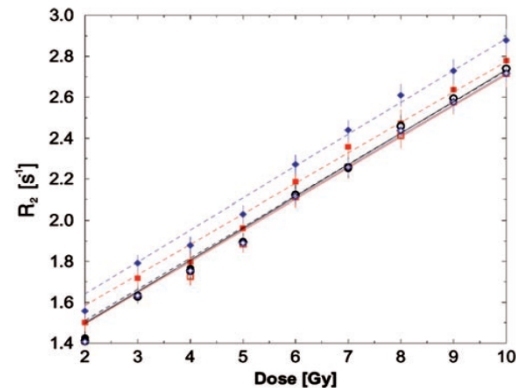


**Figure 19.** Dose- $R_2$  plots measured in three different orthogonal directions. The closed symbols (and dashed lines) are for measurements using an uncompensated standard multi spin echo sequence while the open symbols (and solid lines) are for measurements using a compensated imaging sequence [70].

Before setting up an actual gel dosimetry experiment, it is important to investigate a possible dependence of the acquired  $R_2$  values on imaging direction and other parameters. It is advisable to use a calibration plot that is derived from scans acquired with the same imaging parameters.

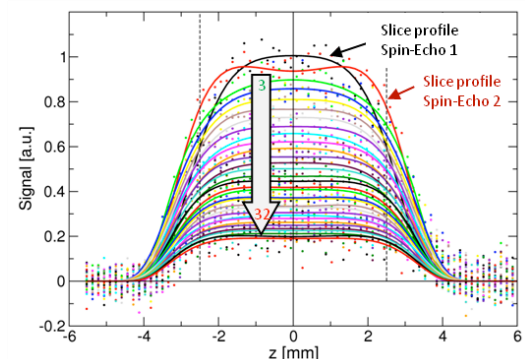


**Figure 20.** Measured slice profiles demonstrate deviations in the first two spin-echo images.

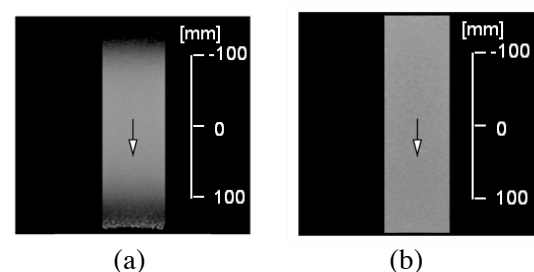


**Figure 21.**  $R_2$  maps of a homogeneous cylindrical gel phantom scanned with the head coil (a) and with the body coil (b).

The  $R_2$  map of the homogeneous phantom is much more uniform when scanned with the body coil (figure 21b). However, measuring  $R_2$  using the body coil as transmitter and receiver is at the cost of signal-to-noise. Modern MRI scanners are equipped with several receive only coils. When still transmitting with the body coil, a good compromise between homogeneity and signal-to-noise can be obtained but this should be used with caution. It is advisable to always scan a homogeneous ('blank') phantom to assess the  $R_2$  homogeneity before scanning an irradiated gel phantom.

**4.3.4. Slice profile imperfections and point-spread function.** The effect of slice profile imperfections has been discussed in connection to eddy currents and  $B_1$  field non-uniformity (figure 20). However, the slice profile also directly affects the spatial information of the dose distribution. As a result of an imperfect slice profile and imaging point-spread function, an outer-voxel contribution will be present in each voxel of the dose distribution. It is important to realize that the outer-voxel contribution depends on imaging parameters. The relative deviation from a rectangular block-shaped slice profile increases as the slice thickness decreases and the in-plane point-spread function (PSF) depends on both the  $T_2^*$  and imaging parameters such as receiver bandwidth, image resolution and phase encoding gradient.

#### 4.4. Object-related dose inaccuracies

**4.4.1. Temperature drift.** The dose- $R_2$  response of polymer gel dosimeters is scanning temperature dependent (figure 22). Any changes or non-uniformities in the temperature distribution during scanning will severely compromise the accuracy of the gel dosimeter phantom.

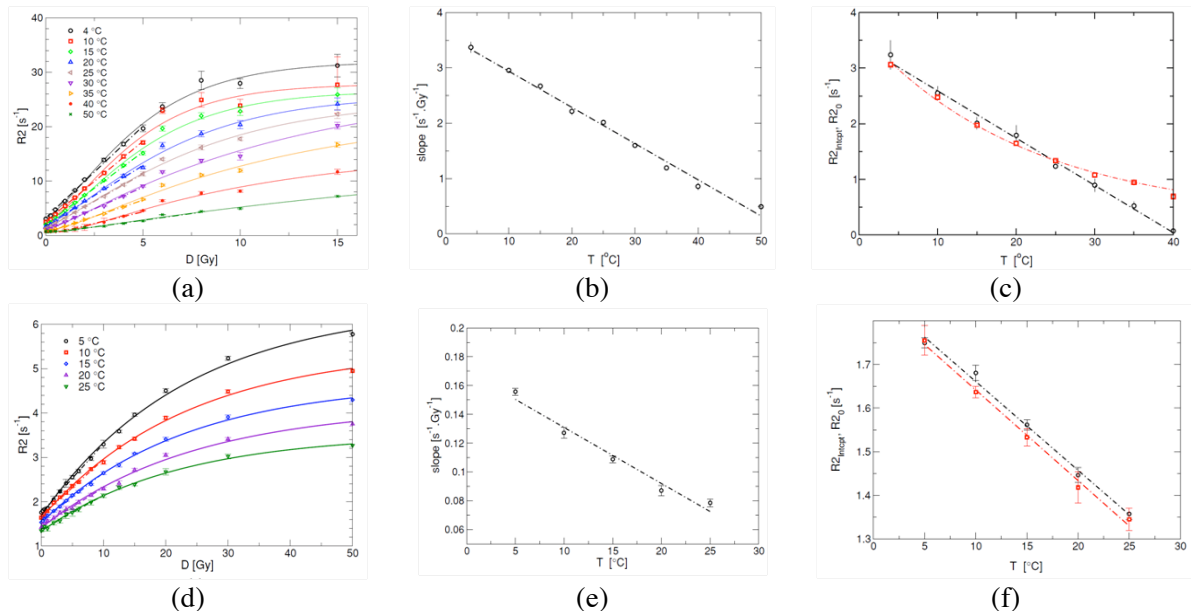


**Figure 22.** Dose- $R_2$  plot of MAGAT (a-c) and PAGAT (d-f) at different scanning temperatures. The slope (b,e) and intercept (c,f) are also plotted.

A systematic dose error will be induced when the calibration vials are at a different temperature than the volumetric GD phantom. With a mono-exponential saturation function as description of the Dose- $R_2$  response:

$$R_2 = R_{2,sat} - \Delta R_2 e^{-\alpha D} \quad (10)$$

the dose error caused by a temperature deviation can be written as:

$$\frac{\partial D}{\partial T} = -\frac{1}{\alpha \Delta R_2} \left( \frac{\partial R_{2,sat}}{\partial T} e^{\alpha D} - \frac{\partial \Delta R_2}{\partial T} + \Delta R_2 D \frac{\partial \alpha}{\partial T} \right) \quad (11)$$

A temperature difference of only 1°C results in a dose error of 0.8 Gy or 8% at a dose of 10 Gy in a PAGAT gel (6 %T) [73]!

The temperature in the scanner room can easily fluctuate in the order of 1°C over a time span of a few hours (figure 23).

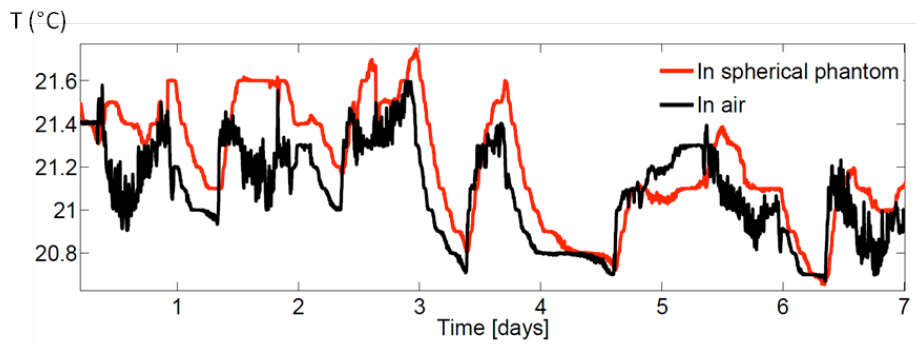


**Figure 23.** Temperature recorded in a scanner room inside a 250 ml spherical phantom (red line) and in air (black line) [73].

Temperature changes in the gel dosimeter may also occur as a result of the heat produced by the absorption of RF energy from the excitation and refocusing pulses. Especially in a 3D dose experiment where more than 30 slices are recorded, the total acquisition time can easily reach several hours and the specific-absorption-rate (SAR) can be substantial [74]. In figure 24, the temperature in the gel phantom during a long scanning experiment is shown.

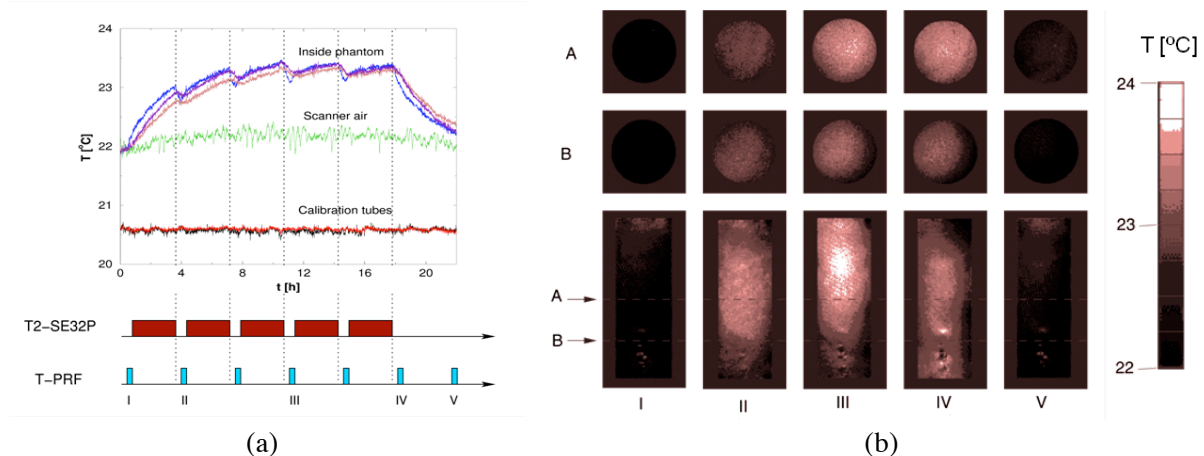


**Figure 24.** (a) Temperature drift during a long-term scanning experiment of a cylindrical gel phantom (length 30 cm × diam. 10 cm). The temperature is recorded by use of a fiber-optic thermometry system with 6 probes. The measurement history is also provided in a corresponding timetable (bottom). (b) Temperature images recorded with the proton resonance frequency (PRF) method at several time points during a multi-echo sequence as indicated in the timetable. The interval between two successive  $R_2$  recordings is approx. 4 hours. The sequence was stopped after the recording of image IV.

Note that a temperature increase is observed during  $R_2$  scanning but not during temperature mapping (FLASH-sequence) illustrating the high-energy transmittance during the multi-echo sequence. The imaging sequence can be made far less sensitive to temperature drift by using a centric k-space ordering scheme instead of a standard k-space linear ordering [74].

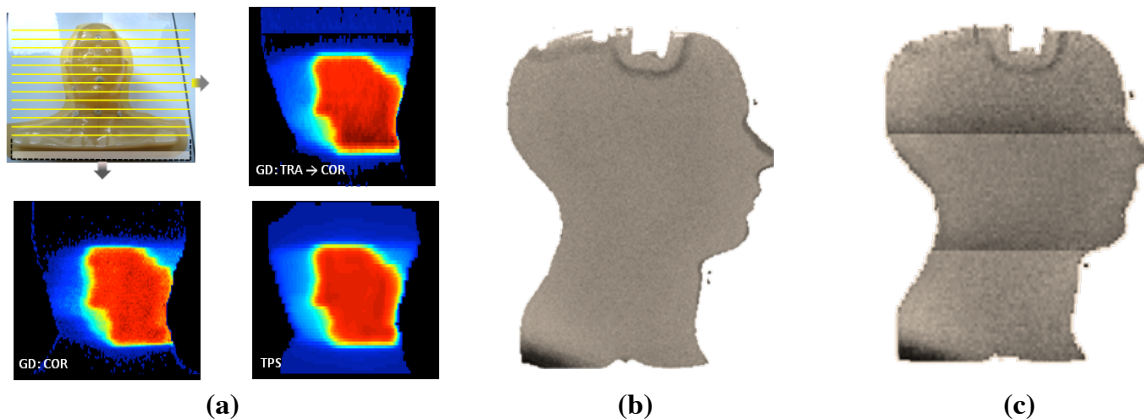


**Figure 25.** Dose deviations in a GD acquired dose distribution were attributed to temperature drift during scanning (a). The effect is clearly demonstrated by comparison of a sagittal R<sub>2</sub> map reconstructed from a transverse set of R<sub>2</sub> maps (b) and a corresponding sagittal R<sub>2</sub> map (c). Transverse scanning was performed in three interleaved blocks.

**4.4.2. Molecular self-diffusion.** A same set of calibration vials but scanned with a different resolution may give a different dose-R2 response. This is partially related to the effect of eddy currents that may be different for a different imaging resolution. However, also the molecular self-diffusion weighting by imaging gradients may have a significant effect especially in high-resolution images [75].

**4.4.4. Magnetic susceptibility induced effects.** As mentioned in section 4.2.1 will differences in magnetic susceptibility between gel, cast material and air create a non-uniform B<sub>0</sub> field. The non-uniform B<sub>0</sub>-field can result in an off resonance effects that create signal voids in the base images. However, the spatial variations in signal are expected to scale with the same factor in all T<sub>2</sub> weighted base images when using a multiple spin echo sequence. As a result no significant effect in the resulting R2 maps will occur (figure 26).

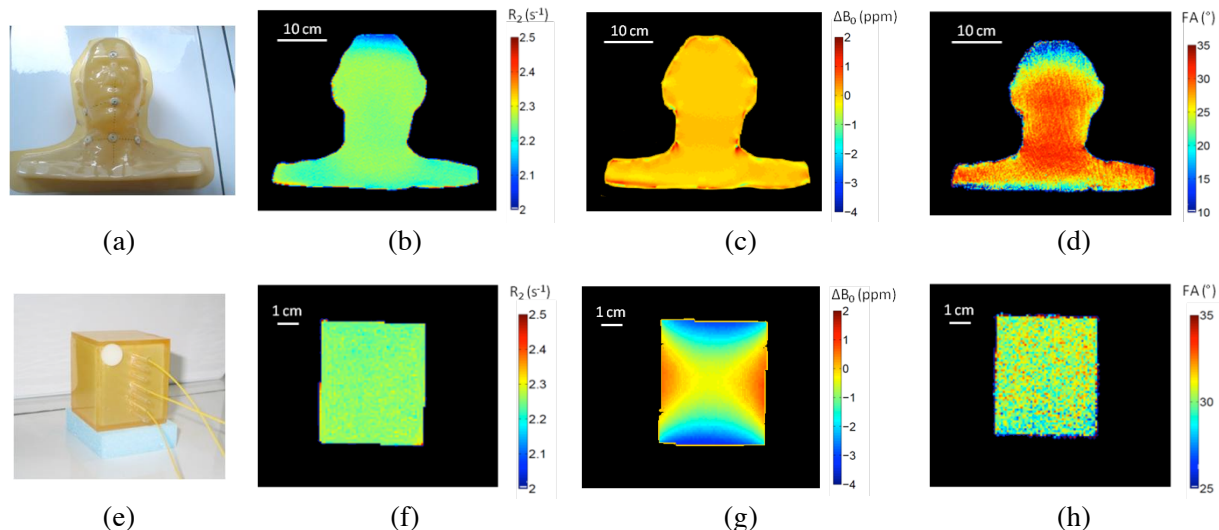


**Figure 26.** Two different blank gel phantoms (a,e) with corresponding R<sub>2</sub> maps (b,f), B<sub>0</sub> field maps (c,g) and B<sub>1</sub> field maps (d,h). No significant correlation between the B<sub>0</sub>-field map and the R<sub>2</sub>-map is observed. The non-uniformity in the cranial area of the humanoid shaped phantom is attributed to the B<sub>1</sub>-field inhomogeneity (d).

However, caution is needed with other imaging sequences or other imaging contrasts such as magnetization transfer (MT) contrast that relies on the saturation of the off-resonance proton pool [76,77].

**4.4.5. Standing waves and dielectric effects.** The attenuation of high-frequency RF waves may be substantial and depends on the dielectric properties of the medium. As the carrier frequency of the RF pulses is proportional with the field strength, the effects may be more pronounced at 3T. When half the wavelength of the RF waves is a multiple of the size of the GD phantom, standing waves may occur [78] in the GD phantom and large  $B_1$  field non-uniformities will be observed (figure 27). Changing the dielectric properties of the phantom by adding salt to the gel, will significantly change the wavelength of the RF waves in the GD phantom thereby improving the uniformity of the  $B_1$  field and  $R_2$  map. The uniformity of the  $R_2$  map of the salt doped gel can be further improved by using a post-processing correction based on an acquired  $B_1$ -field map. The dielectric properties (electrical conductivity and relative dielectric permittivity) of the gel have been measured by use of a network analyser and theoretical calculations in a spherical phantom support the observations [73].

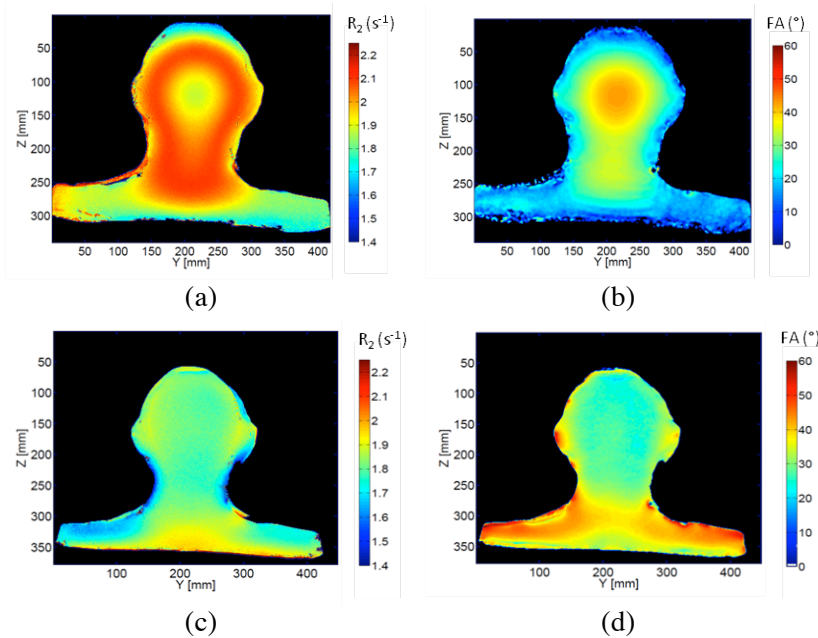


**Figure 27.** Coronal  $R_2$  maps (a,c) and corresponding  $B_1$  field maps (in units of effective flip angle) (b,d) of a conventional blank gel phantom (a,b) and of a salt doped (1% NaCl) gel phantom (c,d) scanned at 3T.

## 6. Relative contributions to the overall uncertainty in polymer gel dosimetry

In table III, the most important contributions to Type B uncertainties are summarized and some realistic values that are common in scanning humanoid shaped PAGAT gel dosimeter phantoms are given. The values listed only serve as typical examples and depend to a large extend on the type of scanner, the shape of the phantom and the coils.

From the overview of sources of uncertainty, it can be concluded that when gel dosimeters are handled under conditions of good practice (see also section 7), the physico-chemical mechanisms should not contribute to more than 2%. Note that for other gel dosimeters (such as MAGAT) where a significantly larger dose rate dependence is found, this figure of uncertainty may be exceeded. Scanner related sources of uncertainty may be kept well below 3 % by a proper scanning setup and/or by applying post-processing compensation methods such as for  $B_0$ - and  $B_1$ -field non-uniformity. A source of uncertainty that has a significant contribution to the overall uncertainty is related to temperature deviations and variations during scanning. These effects can be minimized by use of an imaging sequence with centric k-space reordering and/or an active temperature stabilization using thermal pads or a temperature stabilized water reservoir.

**Table III.** Contribution of different sources of uncertainty estimated on the basis of independent measurements, specifications and calculations for a typical PAGAT gel dosimeter scanned with a multiple spin echo sequence in a clinical MRI.

| Mechanism   | Realistic value        | Estimated uncertainty |
|---|------------------------|-----------------------|
| <b>A. Physico-chemical mechanisms</b>   |                        |                       |
| Storage temperature differences between calibration samples and volumetric gel dosimeter phantom      |                        |                       |
| • Cooling in fridge   | 15 °C (5 h)            | 5 %                   |
| • Slow cooling  | 4 °C (5 h)             | 1 %                   |
| Irradiation temperature (passive temperature stabilization)   | 3 °C                   | 1 %                   |
| Chemical instability (min. 10 h post-irradiation)   |                        |                       |
| • Calibration and volumetric phantom scanned subsequently (4 h): Absolute scanning time difference    | 5 h                    | 2.5 %                 |
| • Calibration and gel dosimeter phantom scanned simultaneously: Absolute scanning time difference     | 1 h                    | 0.5 %                 |
| Spatial integrity: $D_{\max} < 20$ Gy   | -                      | < 1 %                 |
| Dose rate dependence:   | -                      | < 1 %                 |
| Oxygen effect: In glass or Barex recipients   | -                      | < 1 %                 |
| Recipient wall effects  | -                      | < 1 %                 |
| <b>B. Scanning related mechanisms: Spatial distortions</b>  |                        |                       |
| $B_0$ -field non-uniformities: (scanner dependent)<br>for BWpp = 130 Hz                               |                        |                       |
| • Within a spherical volume of 40 cm in a typical 1.5 T   | $\Delta B_0 = 0.5$ ppm | 0.25 pixel            |
| • Within a spherical volume of 50 cm in a typical 1.5 T   | $\Delta B_0 = 2$ ppm   | 1 pixel               |
| Gradient non-linearity  |                        |                       |
| • Within a cylindrical volume (10 cm × 20 cm)   | < 1 %                  | < 1 pixel             |
| Eddy currents   |                        | < 0.5 mm              |
| Magnetic susceptibility differences<br>Note: Spatial correction is possible                           | $\Delta B_0 = 3$ ppm   | 1.5 pixel             |
| Chemical shifts   | -                      | -                     |
| <b>C. Scanning related mechanisms: Dose uncertainties</b>   |                        |                       |
| Eddy currents   |                        |                       |
| • No EC compensation and using non-corresponding calibration set (obtained in another scan direction) | 1 ppm                  | 8 %                   |
| • With EC compensation  | -                      | 1 %                   |
| $B_0$ field non-uniformity  |                        |                       |
| • Within a spherical volume of 40 cm in a typical 1.5 T   | $\Delta B_0 = 0.5$ ppm | < 1 %                 |

|  |  |                                     |
|--|--|-------------------------------------|
| • Within a spherical volume of 50 cm in a typical 1.5 T                            | $\Delta B_0 = 2 \text{ ppm}$   | < 1 %                               |
| B <sub>1</sub> field non-uniformity (Strongly dependent on RF coil)                | $\Delta B_1 = 10 \%$<br>$\Delta B_1 = 20 \%$<br>$\Delta B_1 = 30 \%$<br>$\Delta B_1 = 40 \%$<br>$\Delta B_1 = 50 \%$ | 1.5 %<br>5 %<br>8 %<br>13 %<br>20 % |
| Slice profile imperfections<br>Depends on imaging parameters and dose distribution | -  | -                                   |
| Temperature fluctuations   |  |                                     |
| • Passive setup (without external temperature control)                             | 1 °C   | 8 %                                 |
| • Active temperature control in the scanner (thermal pads)                         | 0.3 °C   | < 3 %                               |
| Temperature drift  |  |                                     |
| • Linear k-space ordering  | 1 °C   | 8 %                                 |
| • Centric k-space ordering   | 1 °C   | < 1 %                               |
| Molecular self-diffusion (scanning direction dependence)                           | -  | -                                   |
| Standing waves and dielectric effects<br>(see B <sub>1</sub> field non-uniformity) | -  | -                                   |

## 7. An independent external calibration of gel dosimeters is possible

The temperature difference between calibration vials and volumetric GD phantom is a major factor of dose uncertainty (Type B). To better control the temperature during scanning, an active temperature controlled experimental setup was applied (figure 28b-c). The GD phantom and calibration vials are wrapped together in a thermal pad through which doped water is send to stabilize and homogenize the temperature in the scanner.

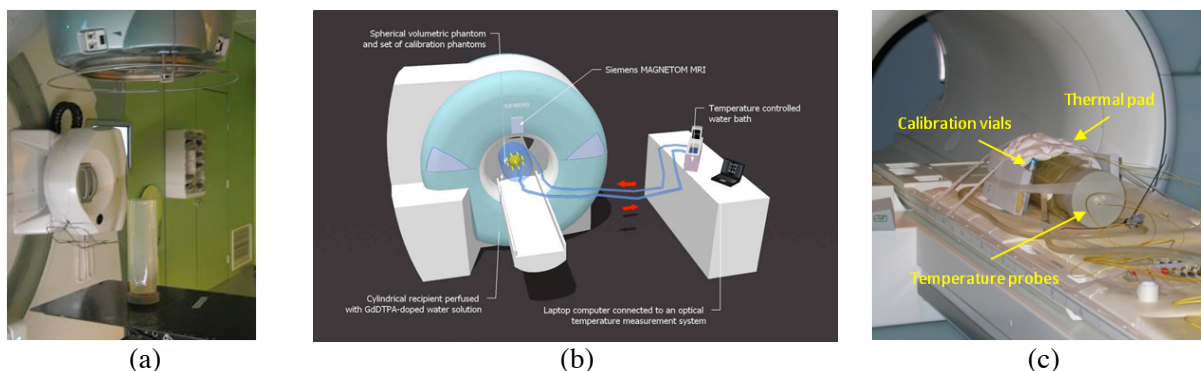


**Figure 28.** Experimental set-up for a temperature-controlled experiment. A 30 cm long volumetric phantom is irradiated with a square 4 cm × 4 cm photon beam (a) and scanned together with calibration tubes that are wrapped in a thermal pad that is connected to a circulating thermostatic water bath (c). The setup shown in (b) is similar to the temperature-controlled setup in (c) but where the spherical phantoms and calibration tubes of the earlier described reproducibility study were placed in a cylindrical recipient that is perfused with contrast agent doped water.

As an illustration of the feasibility of this experimental design we performed some preliminary tests on a 2.5 l cylindrical gel dosimeter phantom that has been irradiated with a 4 cm  $\times$  4 cm square photon beam (figure 28 and 29). A mono-exponential dose- $R_2$  response curve was derived from the calibration vials and used to convert the  $R_2$  maps to a dose map (figure 29b, left:  $R_2$ -map, right: dose-map). A depth-dose curve was extracted from a vertical profile through the dose-map (figure 29c). Within a homogeneous region of 180 mm in the longitudinal direction of the phantom, the dose-difference with an ionization chamber measured dose amounted to less than 5% with most of the points within 3% (see figure 29c and d). The non-uniform dose region beyond 180 cm of the phantom is attributed to a non-uniform  $B_1$ -field. In addition, at the outermost boundary of the phantom (beyond 250 cm from the entrance of the beam), a significant deformation can be observed as a result of a non-uniform  $B_0$ -field. In the results shown in figure 29, no compensation for the non-uniform  $B_0$ - or  $B_1$ -field has been performed.

In several experiments in the past we obtained a similar good agreement between gel dosimeter measured dose distributions and ion chamber measured dose, but in some experiments we found a (Type B) disagreement between the gel measured dose and the ion chamber (see also the tube experiment in figure 16d). We therefore have come to the conclusion that the irreproducibility in earlier experiments was attributed to a systematic temperature difference between calibration samples and the volumetric gel dosimeter phantom. Also, in a retake of the earlier experiment with spherical phantoms but now under temperature-controlled conditions, we found a decrease in dose deviation between gel measured dose and ion chamber measured dose in the centre of the tube to a value well below 3%.

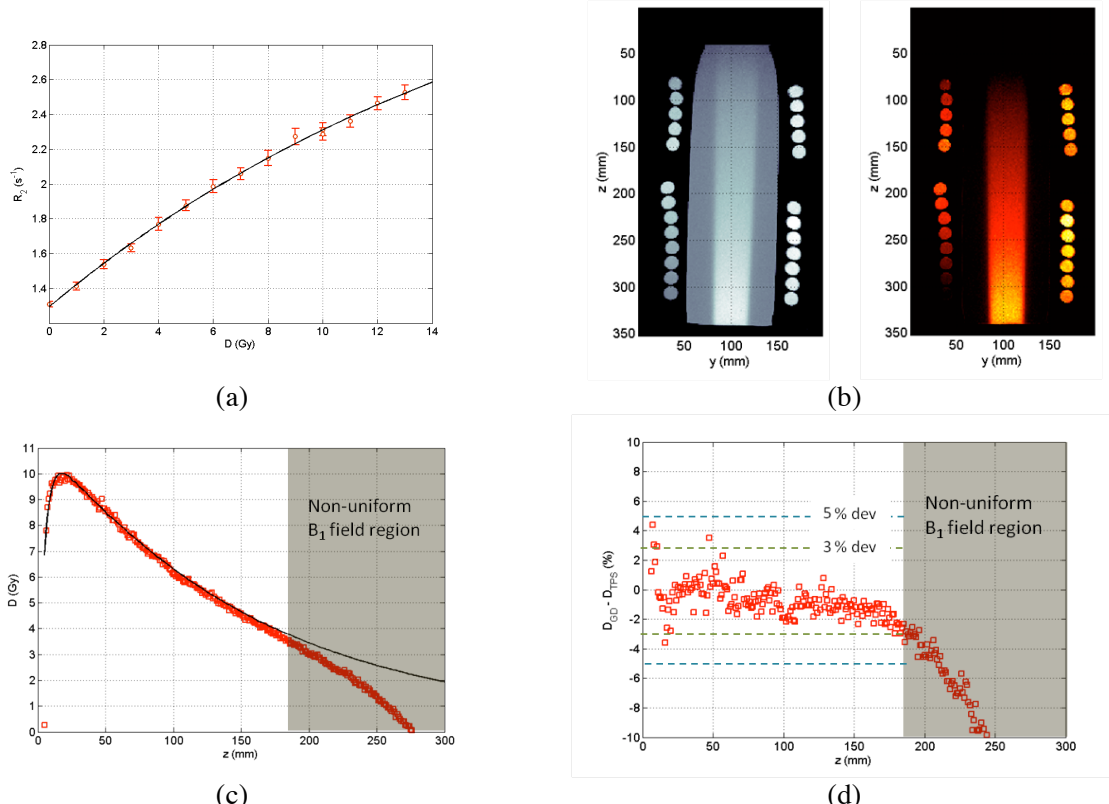


**Figure 29.** A temperature-controlled gel dosimetry experiment with absolute calibration demonstrates excellent agreement of a gel measured depth-dose curve with an ionization chamber measured depth-dose curve. The depth dose curve starts to deviate from the ionization chamber measurement beyond 180 mm as a result of  $B_1$ -field non-uniformity.

## 8. Quick guidelines for good-practice in polymer gel dosimetry with MRI readout

An extensive set of guidelines on how to scan polymer gel dosimeters with MRI has been discussed in previous conference proceedings [77]. Here we summarize it in the shape of a checklist.

|   |  |
|---|--|
| <b>1. Choose a polymer gel dosimeter type</b>   |  |
| <ul style="list-style-type: none"> <li>- Several polymer gel dosimeters have been discussed in the literature or are commercially available, but of only a few types all dosimetric properties have been reported (temperature dependence during irradiation, storage temperature dependence, scanning temperature dependence, dose rate dependence and energy and tissue equivalence). An important parameter is the dose rate dependence as there is no compensation for it.</li> <li>- If the dosimetric properties of the gel dosimeter have not been determined yet, it is advisable to do so.</li> </ul>  |  |
| <b>2. Choose an MR imaging sequence</b>   |  |
| <ul style="list-style-type: none"> <li>- There are several possible sequences and contrast mechanisms that can be used to scan the polymer gel dosimeter, but aside from the dose sensitivity of the imaged parameter, care has to be taken to image uniformity and image distortions.</li> </ul> <p>The most used imaging sequence is a multiple spin-echo sequence by which <math>R_2</math> maps can be obtained.</p> <ul style="list-style-type: none"> <li>- To construct an <math>R_2</math> map from the acquired base images, a pixel-wise fitting algorithm has to be implemented. From the perspective of dose resolution, it is advisable to use an algorithm that is based on the minimization of <math>\chi^2</math>.</li> </ul> |  |
| <b>3. Choose optimal sequence parameters for the polymer gel dosimeter</b>  |  |
| <ul style="list-style-type: none"> <li>- The sequence parameters (such as echo time spacing, number of echoes) can be optimized to yield the best dose-resolution in the parametric map. See the literature [26,27].</li> </ul>   |  |
| <b>4. Construct a cast for the humanoid shaped phantom.</b>   |  |
| <ul style="list-style-type: none"> <li>- The cast is preferably made from Barex, glass or any material with a very low oxygen permeability coefficient to minimize the infiltration of oxygen in the gel dosimeter.</li> </ul>  |  |
| <b>5. Fill the cast with a blank(non-irradiated) gel phantom.</b>   |  |
| <ul style="list-style-type: none"> <li>- Use a gel composition that has similar MRI properties as the gel to be used for the actual dosimetry (e.g. a gelatine gel doped with contrast agent and/or anti-fungicide).</li> <li>- Provide the phantom with fiducial markers that will be later visible on CT and MR images.</li> </ul>  |  |
| <b>6. Scan the blank phantom with CT and perform treatment planning on the scanned data set.</b>  |  |
| <ul style="list-style-type: none"> <li>- PTV and OARs are virtually created on the basis of realistic anatomy</li> </ul>  |  |
| <b>7. Scan the blank phantom and determine uniformity, distortion and signal-to-noise.</b>  |  |
| <ul style="list-style-type: none"> <li>- This is a vital step which is often overlooked.</li> <li>- The blank phantom should be scanned with similar parameters as will be used for scanning the actual gel dosimeter phantom.</li> </ul>   |  |

|  |  |
|--|--|
| <ul style="list-style-type: none"> <li>- During this investigative procedure, compensation strategies can be implemented.</li> </ul>   |  |
| <p><b>8. Fabricate polymer gel</b></p> <ul style="list-style-type: none"> <li>- Control temperature during fabrication and storage</li> </ul>  |  |
| <p><b>9. Perform the polymer gel dosimetry experiment</b></p> <ul style="list-style-type: none"> <li>- Dose prescription and beam data transported to Linac</li> <li>- Maximum dose scaled to limits determined by spatial integrity limit</li> <li>- Alignment of phantom on the basis of line markers, fiducial markers or additional immobilization device (in conformity with patient treatment)</li> <li>- Stabilize temperature in the gel dosimeter by use of thermal pads or circulating water reservoir before and during scanning.</li> <li>- (Acquire <math>B_0</math>- and/or <math>B_1</math>-field map for compensation of non-uniformities.)</li> </ul> |  |
| <p><b>10. Compare the GD derived dose maps with TPS</b></p> <ul style="list-style-type: none"> <li>- Use gamma analysis carefully to avoid bias as a result of image noise (i.e. Use gel derived dose distribution as reference and TPS as evaluator)</li> </ul>   |  |

## References

- [1] Baldock C *et al* 2010 *Phys. Med. Biol.* **55** R1–63
- [2] Vergote K *et al* 2004 *Phys. Med. Biol.* **49** 287–305
- [3] De Deene Y *et al* 2000 *Magn. Reson. Med.* **43** 116–25
- [4] Dumas E *et al* 2006 *J. Phys.: Conf. Ser.* **56** 239–41
- [5] MacDougall N D *et al* 2008 *Br. J. Radiology* **81** 46–50
- [6] De Deene Y *et al* 2007 *Phys. Med. Biol.* **52** 2719–28
- [7] Cosgrove V P *et al* 2000 *Phys. Med. Biol.* **45** 1195–210
- [8] Sedaghat M *et al* 2011 *Phys. Med. Biol.* **56** 6083–107
- [9] De Deene Y *et al* 1998 *Radiother. Oncol.* **48** 283–91
- [10] Haraldsson P *et al* 2000 *Br. J. Radiol.* **73** 58–65
- [11] Pappas E *et al* 2001 *Phys. Med. Biol.* **46** 783–97
- [12] Ibbott G S *et al* 1997 *Int. J. Radiat. Oncol. Biol. Phys.* **38** 1097–103
- [13] Oldham M *et al* 1998 *Phys. Med. Biol.* **43** 1113–32
- [14] Meeks S L *et al* 1999 *Int. J. Radiat. Oncol. Biol. Phys.* **43** 1141–53
- [15] Cosgrove V P *et al* 2000 *Phys. Med. Biol.* **45** 1195–210
- [16] Ramm U *et al* 2000 *Phys. Med. Biol.* **45** N95–102
- [17] Farajollahi A R *et al* 2000 *Phys. Med. Biol.* **45** N9–N14
- [18] Grebe G *et al* 2001 *Int. J. Radiat. Oncol. Biol. Phys.* **49** 1451–60
- [19] De Deene Y 2006 *J. Phys.: Conf. Ser.* **56** 72–85
- [20] Low D A *et al* 1998 *Med. Phys.* **25** 656–661
- [21] Jiang S B *et al* 2006 *Phys. Med. Biol.* **51** 759–776
- [22] Meeks S L *et al* 1999 *Int. J. Radiat. Oncology Biol. Phys.* **43** 1135–1141
- [23] De Deene Y *et al* 2006 *Phys. Med. Biol.* **51** 653–673
- [24] Karlsson A *et al* 2007 *Phys. Med. Biol.* **52** 4697–706
- [25] De Deene Y *et al* 2002 *Phys. Med. Biol.* **47** 2459–2470
- [26] De Deene Y *et al* 1998 *Signal Processing* **70** 85–101
- [27] De Deene Y and Baldock C 2002 *Phys. Med. Biol.* **47** 3117–3141
- [28] Vandecasteele J and De Deene Y 2013 *Phys. Med. Biol.* **58** 19–42

- [29] Vandecasteele J and De Deene Y 2013 *Phys. Med. Biol.* **58** 43-61
- [30] Salomons G J *et al* 2002 *Phys. Med. Biol.* **47** 1435-48
- [31] De Deene Y *et al* 2000 *Phys. Med. Biol.* **45** 859-878
- [32] Lepage M *et al* 2001 *Phys. Med. Biol.* **46** 2827-39
- [33] Olsson L E *et al* 1990 *Phys. Med. Biol.* **35** 1623-1631
- [34] Kron T *et al* 1997 *Magn. Reson. Imaging* **15** 211-221
- [35] Harris P J *et al* 1996 *Phys. Med. Biol.* **41** 1745-1753
- [36] De Deene Y *et al* 2001 *Phys. Med. Biol.* **46** 2801-2825
- [37] Vergote K *et al* 2004 *Phys. Med. Biol.* **49** 4507-4522
- [38] Fuxman A M *et al* 2005 *Chem. Eng. Science* **60** 1277-93
- [39] Jirasek A and Duzenli C 2002 *Med. Phys.* **29** 569-77
- [40] Fong P M *et al* 2001 *Phys. Med. Biol.* **46** 3105-13
- [41] Hepworth S J *et al* 1999 *Phys. Med. Biol.* **44** 1875-84
- [42] Sedaghat M *et al* 2011 *Phys. Med. Biol.* **56** 601-25
- [43] Michael G J *et al* 2000 *Phys. Med. Biol.* **45** N133-N138
- [44] Baldock C *et al* 2001 *Phys. Med. Biol.* **46** 449-60
- [45] De Deene Y 2004 *J. Phys.: Conf. Series* **3** 87-114
- [46] De Deene Y 2009 *J. Phys.: Conf. Ser.* **164** 012033
- [47] Oldham M and Kim L 2004 *Med. Phys.* **31** 1093-1104
- [48] Xy Y and Wuu C-S 2004 *Med. Phys.* **31** 3024-3033
- [49] Doran S J and Krstajic N 2006 *J. Phys.: Conf. Ser.* **56** 45
- [50] Doran S J 2010 *J. Phys.: Conf. Ser.* **250** 012086
- [51] Price R R *et al* 1990 *Med. Phys.* **17** 287- 95
- [52] Michiels J *et al* 1994 *Magn. Reson. Imaging* **12** 749-65
- [53] Schad L R *et al* 1992 *Magn. Reson. Imaging* **10** 609-21
- [54] Doran S J *et al* 2005 *Phys. Med. Biol.* **50** 1343-61
- [55] Cho Z H *et al* 1988 *Med. Phys.* **15** 7-11
- [56] De Deene Y *et al* 2000 *Phys. Med. Biol.* **45** 1807-23
- [57] Jehenson P *et al* 1990 *J. Magn. Reson.* **90** 264-78
- [58] Ahn C B and Cho Z H 1991 *IEEE Trans. Med. Imag.* **10** 47-52
- [59] Wysong R E and Lowe I J 1991 *Magn. Reson. Med.* **17** 149-63
- [60] Ahn C B and Cho Z H 1991 *Magn. Reson. Med.* **17** 149-63
- [61] Liu Q *et al* 1994 *Magn. Reson. Med.* **31** 73-6
- [62] Boesch C H *et al* 1991 *Magn. Reson. Med.* **20** 268-84
- [63] Robertson S *et al* 1992 *Magn. Reson. Med.* **25** 158-66
- [64] Schiff J *et al* 1994 *J. Magn. Reson. Series B* **104** 73-6
- [65] Collins C M *et al* 2002 *Magn. Reson. Imaging* **20** 413-24
- [66] Li S *et al* 1996 *Magn. Reson. Med.* **36** 705-14
- [67] Park H W *et al* 1988 *Phys. Med. Biol.* **33** 339-49
- [68] Crijns S P M *et al* 2011 *Phys. Med. Biol.* **56** 289-97
- [69] Holland D *et al* 2010 *Neuroimage* **50** 175-83
- [70] De Deene Y *et al* 2001 *Phys. Med. Biol.* **46** 2801-25
- [71] Fransson A *et al* 1993 *Magn. Reson. Imaging* **11** 771-84
- [72] De Deene Y *et al* 2000 *Phys. Med. Biol.* **45** 1825-39
- [73] Vandecasteele J and De Deene Y 2013 *Phys. Med. Biol.* **58** 63-85
- [74] De Deene Y and De Wagter C 2001 *Phys. Med. Biol.* **46** 2697-711
- [75] Hurley C *et al* 2003 *Phys. Med. Biol.* **48** 3043-58
- [76] Lepage M *et al* 2002 *Phys. Med. Biol.* **47** 1881-90.
- [77] De Deene Y *et al* 2006 *Med. Phys.* **33** 2586-97.
- [78] Tofts P S 1994 *J. Magn. Res. Ser. B* **104** 143-7
- [79] De Deene Y 2010 *J. Phys.: Conf. Ser.* **250** 012015